7-27-2015

The Life Cycle of Instability Features Measured from the Andes Lidar Observatory Over Cerro Pachon on 24 March 2012

J. H. Hecht
The Aerospace Corporation

K. Wan
University of Illinois at Urbana-Champaign, Urbana, Illinois

Lynette Gelinas
The Aerospace Corporation

David Fritts
University of Illinois at Urbana-Champaign, Urbana, Illinois,

R. L. Walterscheid
The Aerospace Corporation

See next page for additional authors

Scholarly Commons Citation

Hecht, J. H., Wan, K., Gelinas, L., Fritts, D., Walterscheid, R. L., Rudy, R. J., Liu, A., Franke, S. J., Vargas, F., Pautet, P. -., Taylor, M., & Swenson,, G. (2015). The Life Cycle of Instability Features Measured from the Andes Lidar Observatory Over Cerro Pachon on 24 March 2012. *Journa lof Geophysical Research: Atmospheres, 119*(14). https://doi.org/10.1002/2014JD021726

AGU PUBLICATIONS

JGR

Journal of Geophysical Research: Atmospheres

RESEARCH ARTICLE

10.1002/2014JD021726

This article is a companion to *Fritts et al.* [2014] doi:10.1002/2014JD021737.

Key Points:
- Instabilities showed the formation of secondary instabilities
- Features were present in the buoyancy subrange
- Simulations show features with sizes comparable to what is seen in the images

Supporting Information:
- Readme
- Movie S1

Correspondence to:
J. H. Hecht,
james.hecht@aero.org

Citation:
Hecht, J. H., et al. (2014), The life cycle of instability features measured from the Andes Lidar Observatory over Cerro Pachon on March 24, 2012, *J. Geophys. Res. Atmos.*, *119*, 8872–8898, doi:10.1002/2014JD021726.

Received 6 MAR 2014
Accepted 7 JUL 2014
Accepted article online 12 JUL 2014
Published online 31 JUL 2014

The life cycle of instability features measured from the Andes Lidar Observatory over Cerro Pachon on 24 March 2012

J. H. Hecht[1], K. Wan[2], L. J. Gelinas[1], D. C. Fritts[2], R. L. Walterscheid[1], R. J. Rudy[1], A. Z. Liu[3], S. J. Franke[4], F. A. Vargas[4], P. D. Pautet[5], M. J. Taylor[3], and G. R. Swenson[4]

[1]Space Science Applications Laboratory, The Aerospace Corporation, El Segundo, California, USA, [2]Department of Electrical and Computer Engineering, University of Illinois at Urbana-Champaign, Urbana, Illinois, USA, [3]Department of Physical Sciences, Embry-Riddle Aeronautical University, Daytona Beach, Florida, USA, [4]Center for Atmospheric and Space Sciences, Utah State University, Logan, Utah, USA, [5]GATS Inc, Boulder, Colorado, USA

Abstract The Aerospace Corporation's Nightglow Imager (ANI) observes nighttime OH emission (near 1.6 μm) every 2 s over an approximate 73° field of view. ANI had previously been used to study instability features seen over Maui. Here we describe observations of instabilities seen from 5 to 8 UT on 24 March 2012 over Cerro Pachon, Chile, and compare them with previous results from Maui, with theory, and with Direct Numerical Simulations (DNS). The atmosphere had reduced stability because of the large negative temperature gradients measured by a Na lidar. Thus, regions of dynamical and convective instabilities are expected to form, depending on the value of the Richardson number. Bright primary instabilities are formed with a horizontal wavelength near 9 km and showed the subsequent formation of secondary instabilities, rarely seen over Maui, consistent with the primaries being dynamical instabilities. The ratio of the primary to secondary horizontal wavelength was greater over Chile than over Maui. After dissipation of the instabilities, smaller-scale features appeared with sizes in the buoyancy subrange between 1.5 and 6 km. Their size spectra were consistent with the model of Weinstock (1978) if the turbulence is considered to be increasing. The DNS results produce secondary instabilities with sizes comparable to what is seen in the images although their spectra are somewhat steeper than is observed. However, the DNS results also show that after the complete decay of the primary features, scale sizes considerably smaller than 1 km are produced and these cannot be seen by the ANI instrument.

1. Introduction

The mesopause region of the Earth's atmosphere, which occurs nominally between 80 and 100 km in altitude, not only has the coldest temperatures of the Earth's system but it is also a very interesting natural laboratory for the study of fluid dynamic processes. Large-amplitude diurnal and semidiurnal tides often exist, producing large wind shears and steep negative temperature gradients. These in turn can render the atmosphere unstable, producing convective (superadiabatic lapse rate) and Kelvin-Helmholtz (wind shear) instabilities. These instabilities ultimately break down, and the end product of instabilities is turbulence, leading to increased eddy diffusion rates, which affects the distribution of mesosphere and lower thermosphere constituents such as atomic oxygen (e.g., NASA TOMEX campaign discussed in the work of *Hecht et al.* [2004b] and *Liu et al.* [2004]) and Na [*Liu*, 2009; *Gardner and Liu*, 2010]. Thus, an understanding of instability life cycles is important for an accurate modeling of the mesopause region.

The Kelvin-Helmholtz instability (KHI) has been known for over 100 years, and an earlier paper by *Fritts et al.* [1996] cites many of the important papers published to date on this phenomenon. The criterion applicable to the atmosphere is that when the Richardson number (*Ri*), defined as ratio of the square of the Brunt-Väisälä frequency to the square of the wind shear [*Richardson*, 1920], is less than 0.25 the atmosphere becomes dynamically unstable, and a region of Kelvin-Helmholtz billows may form [e.g., *Miles and Howard*, 1964; *Scorer*, 1969; *Gossard and Hooke*, 1975; *Chandrasekhar*, 1981]. Many of the billow features such as horizontal wavelength and height depend on the vertical extent of the unstable region. The lifetime and evolution of these billows and their subsequent dissipation and formation of turbulence are far less understood [e.g., *Fritts et al.*, 1996]. Yet the mixing of atmospheric species by the formation of KHI billows, and the resulting turbulence is important in understanding the structure of the atmosphere in the upper mesosphere and lower thermosphere.

A convective instability (CI) occurs when the temperature lapse rate is superadiabatic, causing *Ri* to be negative. It was not fully understood as to how this could be realized in the atmosphere since *Ri* would always be less than 0.25 and positive before becoming negative. *Fritts et al.* [1997] investigated this and showed that the growth rates for the respective instabilities were such that the growth rate of a CI is fast enough that it can preempt the formation of a KHI.

Numerical modeling studies have been used for furthering the understanding of the fine structure and physics of the evolution and breakdown of a KHI. A 2-D simulation by *Klaassen and Peltier* [1985a] followed the evolution of KHIs and suggested that for flows with Reynolds number on the order of 500, a secondary convective instability existed, which should lead to the formation of convective rolls. The existence of these secondary structures, which were predicted to be convectively unstable, was anticipated by observations in the ocean [*Woods*, 1969; *Orlanski and Bryan*, 1969] and by the hypothesis of *Davis and Peltier* [1979] that buoyancy-induced instabilities would form in the core of the KHI vortex and produce shear-aligned convective rolls perpendicular to the main KHI billow structures. These secondary structures are best modeled, though, by 3-D simulations. Klaasen and Peltier used partly 3-D numerical simulations that revealed the formation of secondary convective instabilities and their breakdown into turbulence [*Klaassen and Peltier*, 1985b, 1991]. As computing power became greater, fully 3-D Direct Numerical Simulations (DNS) occurred allowing a more realistic look at the evolution of KHIs in general and the secondary instability in particular [*Palmer et al.*, 1994; *Fritts et al.*, 1996; *Palmer et al.*, 1996; *Werne and Fritts*, 1999; *Caulfield and Peltier*, 2000; *Peltier and Caulfield*, 2003]. Note, however, that classical instability conditions may be modified by the wave-induced variation of the background seen by these structures [*Klostermeyer*, 1990; *Fritts et al.*, 2009]. It is still an open question as to how well modeling describes the real atmosphere in the presence of these instabilities.

Observations and laboratory experiments have also been used to further understand KHI breakdown. While observations of KHI billow, formation has been made in the lower atmosphere [e.g., *Browning and Watkins*, 1970], the reality of these modeling results has only partially been tested by comparison with experiments [*Thorpe*, 1985]. Laboratory studies pioneered by *Thorpe* [1968] indeed suggested that KHI billows do evolve secondary instabilities that precede the decay into turbulence [e.g., *Thorpe*, 1973]. However, some laboratory observations have been hampered by wall effects [*Thorpe*, 1985, 1987] and it has not been confirmed that the evolution of the KHI primary and secondary instabilities observed in such experiments actually occurs in the atmosphere. Thus, the physics of the breakdown of the KHI structures in the atmosphere is not well elucidated by these experiments.

The Earth's airglow originates in the mesopause region, at altitudes where KHIs and CIs naturally occur. One of the earliest results of airglow imaging studies was the observation of so-called ripple structures, named after their resemblance to ripples on a pond. These are wavelike features that resemble atmospheric gravity waves (AGWs) in appearance but have short horizontal wavelengths (<15 km) and short lifetimes (a few tens of minutes) [e.g., *Peterson and Kieffaber*, 1973; *Peterson*, 1979; *Taylor and Hapgood*, 1990; *Taylor and Hill*, 1991; *Taylor et al.*, 1997; *Hecht et al.*, 1997, 2000]. Work reviewed by *Hecht* [2004a] concluded that ripples are not AGWs but rather the manifestation of KHIs or CIs. Thus, in principle, OH airglow ripple observations can be used to study KHI and CI evolution.

Indeed, several studies on the nature of ripples were conducted from Mount Haleakala on Maui using an airglow infrared imaging camera developed by The Aerospace Corporation and associated instrumentation that was part of the Maui-MALT campaign. One set of studies investigated the probability that KHIs or CIs would form over Mount Haleakala, essentially a mid-Pacific site. *Hecht et al.* [2007] showed that at Maui, ripples occurred 10 to 20% of the time with atmospheric conditions, as measured by a Na lidar, more favorable to the formation of KHIs rather than CIs. Mesospheric stability conditions calculated with the lidar data at Maui also support that the probability of KHI occurrence is 9–10%, whereas a CI occurs 2–3% of the time [*Li et al.*, 2005a].

These studies support the notion that OH airglow can study in detail the formation of KHIs and or CIs, and one Maui-MALT study did investigate the life cycle of a KHI. *Hecht et al.* [2005] followed the life history of an instability feature from observations during the night of 15 July 2002, and the results supported the interpretation that it was a KHI. But there was both agreement and disagreement with model predictions of KHI formation and decay. In particular, the prediction for the convective decay of KHI ripples was at odds with the data. Models predict horizontal wavelengths for the secondary CIs that were shorter than observed.

Table 1. Data Sources[a]

Name (Type)	Product	Altitude (km)	Field of View (deg)	Horizontal Pixel	Vertical Pixel	Cadence
ANI (Camera)	OHBI 256 × 256 pixels	87	70	0.5 km	na	2 s
MTM (Camera)	OHTI	87	90	0.5 km	na	1 min
MCP (Photometer)	OI (557.7 nm) counts	97	3	na	na	≈2 min
MR (Radar)	Horizontal wind	80–100	120	na	3 km	60 min
Na Lidar	Temperature	80–105	0.057	na	500 m	15 min

[a]ANI = The Aerospace Corporation's Nightglow Imager, MTM = Mesospheric Temperature Mapper, MCP = multichannel photometer, MR = meteor radar, OHBI = OH Brightness Image (see text), OHTI = OH Temperature Image, na = not applicable.

Subsequent observations (to be presented in a future work) suggested that observations over Maui of the formation of secondary instabilities in KHIs and the decay of KHIs into smaller-scale structures were both very rare. With only observations over a mid-ocean site it was not possible to determine if the lack of secondary formation was unique to the atmosphere over the site and whether the differences between the 15 July 2002 observations and the model represented real problems with the model predictions.

The investigation discussed here was carried out at the newly established Andes Lidar Observatory (ALO) at Cerro Pachn (30.3°S, 70.7°W, 2530m) in northern Chile. This location produces what may be the purest examples of terrain-generated waves due to the extreme dryness of the area and minimal convective activity over Chilean coastal waters to the west. Furthermore, it is a region of steep terrain and a prolific generator of waves over a wide range of frequencies, from stationary mountain waves to high-frequency waves generated by gusty winds [*Walterscheid and Hickey*, 2005]. Such waves when combined with large-amplitude background tides, which predispose the atmosphere to being unstable, might be expected to produce frequent instability events [*Hecht et al.*, 2004c; *Liu et al.*, 2004]. As ALO is a true mountain site, it is anticipated there would be significant differences with what was observed over Maui. ALO includes many of the instruments previously located at Mount Haleakala including the airglow infrared imaging camera, a Na wind temperature lidar, a meteor radar, and additional airglow imagers. The airglow infrared camera has been operating since late 2009, and the images reveal frequent formation of KHIs and secondary instabilities. A climatology of such features will be reported in a subsequent study.

In March 2012 Na lidar temperature observations began and this paper reports on a study of the lifetime of instabilities analogous to the Maui study. In particular, we will present observations made on the evening of 23–24 March 2012 with a special emphasis on the 5 to 7 UT period on 24 March where strong ripple formation was seen in the image data. These observations will be analyzed using three different techniques. The image entropy technique allows a quantitative measure of the nonuniformity on image. This will allow identification of periods where small horizontal scale ripples or turbulent-like structures are visible. The fast Fourier transform (FFT) analysis will allow a determination of the horizontal wavelengths of any turbulent or ripple structures. The wavelet analysis will allow a measure of the periodicity of the ripple or turbulent features. Finally, these results will be compared to numerical model predictions to see whether there is the same disagreement as was reported from Maui.

2. Experimental Instrumentation and Models

Table 1 summarizes the attributes of the instruments used in this study.

2.1. Instrument Descriptions

2.1.1. ANI

The Aerospace Corporation's near-IR camera (ANI) is described in some detail in *Hecht et al.* [2005] for its operation during Maui-MALT. There have only been a few changes for its operation at ALO. The camera has a wide-angle lens with a 256 × 256 HgCdTe detector array to provide images over an ≈ 73 × 73° region of the sky. In an image, 128 pixels across the center is approximately equal to 40°, or 61 km, at 85 km altitude. The array consists of four 128 × 128 quadrants each with their own readout circuitry. A new detector was purchased prior to installation at ALO so that all four quadrants are now operational. A fixed open filter position is used allowing a spectral range (1.55–1.7 μm) determined by the internal filters to be imaged. This spectral range is dominated by the OH Meinel airglow, and because the OH Meinel (4,2) band brightness is almost 100 kRy, the signal to noise (S/N) for a 1 s integration is over 200:1. There is some geometric distortion in

the images especially near the edge of images in that straight lines appear somewhat curved. Stars moving across the image from east to west move in somewhat curved lines away from the center pixels. The alignment of the imager with respect to geographic north and east is somewhat changed from *Hecht et al.* [2005] as the camera is located in a new observatory. Here north is nominally at the top of each image while east is to the left and west the right.

At ALO, images are exposed for about 1 s and images are obtained approximately every 2 s. For this work, data are taken in this mode for all but about 10 s per hour. For those last 10 s, a shutter is closed and dark images are taken. These dark images are typically about a factor of 30 or more less intense than the airglow image. They are not subtracted from the raw images. The data from the images are presented as digital counts. The nominal read noise for the chip is about 30 electrons.

However, some further processing of the images are performed for this study following previous work [*Hecht et al.*, 2005]. Each raw image can be normalized or flatfielded by dividing the raw image by the average of images taken over the whole night, a normalization image. Before normalizing, owing mainly to the camera optics, the brightest part of each image is the center and the edges are dim, and thus, it is difficult to see low contrast features. However, features present in the normalization image can show up as a fixed pattern in the normalized images. Thus, it is important to show (or analyze) a sequences of images and look for changes between images.

A better way to bring out the contrast in, and study the evolution of, faint moving structures is to apply the image difference approach. In this approach, successive images are subtracted. This acts as a high pass filter, allowing the observation of any feature that changes and eliminating features fixed with respect to the time difference. No normalization or flatfielding is used in this approach. If the time interval between the images used for differencing was equal to the time it takes for the bright features to travel one wavelength (one wave period), then the resultant difference image for a monochromatic wave would yield a zero signal. However, if the time difference is equal to one half of a wave period, then the signal level will appear to be both positive and negative. For this study, difference images are formed by subtracting raw images taken either 30 s or 60 s apart which were found to be optimal. Times shorter than 30 s or longer than 60 s resulted in too much filtering of the ripples because the ripples have not moved far enough in 30 s or may start to be aliased for times longer than 60 s. Reference to either or both of these time differences is presented in the following sections. In general, though 60s differences produced better looking images and thus are used for the movie, the image presentation, and the entropy analysis. The 30 s differences were better for the FFTs since that filters out more of the longer wavelength structures as discussed in that section.

Although each image has 256×256 pixels the analysis will also use data from six separate square box regions in each image. Each region is 64×64 pixels, and there are three equally spaced columns and two equally spaced rows of these regions.

2.1.2. University of Illinois at Urbana-Champaign Na Wind and Temperature Lidar

The University of Illinois at Urbana-Champaign (UIUC) Na lidar as operated during Maui-MALT was also described in *Hecht et al.* [2005]. However, for operation at ALO, the receiver system was modified extensively and this is partly described in *Carlson et al.* [2005]. Although both horizontal wind and temperature can be measured at ALO, on this night only temperature data are available because the lidar was pointed in the zenith direction. The temperature profiles were calculated using photon count profiles with a 90 s integration and a 500 m vertical resolution.

2.1.3. UIUC MR

Wind data are available from the UIUC meteor radar (MR) located at the base of Cerro Pachon. This instrument is fully described in *Franke et al.* [2005]. A single three-element Yagi antenna directed toward the zenith is used to illuminate meteor trails. Meteor trail reflections are coherently detected on five three-element Yagi antennas oriented along two orthogonal baselines, with one antenna in the center of the array common to both baselines. On each baseline the outer antennas are separated from the center antenna by 1.5 and 2.0 wavelengths. This configuration minimizes antenna coupling, provides enough redundancy to unambiguously determine the azimuth and elevation of most echoes, and provides excellent angular resolution for position determination. For this study, points are provided every half hour in the altitude range 80–100 km and sampled every 1 km. The altitude resolution of these estimates is determined by a triangular weighting function with half width of 3 km and base width of 6 km.

2.1.4. UIUC MCP

To determine the vertical extent of the AGW activity, some data are used from the UIUC multichannel photometer (MCP). The MCP simultaneously measures three airglow emissions OH Meinel (5–1), (6–2), 840 nm; O_2 (b) (0,1), 865 nm; and O(^1S), 557.7 nm, which typically originate from approximately 87 km, 92 km, and 94 km, respectively [*Vargas et al.*, 2007]. Each channel has a bandpass interference filter to allow emissions to be measured with a photomultiplier tube module and a data acquisition card via photon counting. An integration time of 5 s is used, and data are obtained every 5 s. For this study though, only data from the OI (557.7 nm) channel are used.

2.1.5. Utah State University MTM

To determine the temperature perturbations induced by atmospheric gravity wave activity, some data are used from the Utah State University Mesospheric Temperature Mapper (MTM) that has been designed to measure the mesospheric OH (6,2) and O_2 (0,1) rotational temperatures over a 90° field of view, centered on the zenith. It uses a back-illuminated 1024 × 1024 pixel CCD detector that is binned down to 128 × 128 pixels to improve the sensitivity, a Keo Scientific telecentric lens system, and a set of narrowband interference filters to measure the P12 and P14 lines of the OH (6,2) band and the sky background (BG) intensity at 857 nm [*Taylor et al.*, 2001]. In addition, this instrument also measures the intensity of two emission lines of the atmospheric O_2 (0,1) band. For this study though, the O_2 data were not used. The other three filters (P12, P14, and BG) were exposed for 30 s each, providing a temperature map every 1.75 min. A keogram is also made using the OH (6,2) band intensity images, which is a combination of the three filters. The zenith temperature data, obtained by dividing the background-corrected OH filter images, correspond to the average of a small 5 × 5 pixels area (approximately 4 × 4°).

This instrument has performed extremely well during the past 15 years: at Fort Collins, CO (40.5N), at the Starfire Optical Range, NM (35N), at the Bear Lake Observatory, UT (41.9N), at the Maui Observatory, HI (20.8N) during 5 years as part of the Maui-MALT program, and since 2009 at the Cerro Pachon, Chile (30.3°S) ALO site. The extensive data sets obtained by the MTM have been used to study long-term temperature variations [*Zhao et al.*, 2005] as well as tidal oscillations [*Taylor et al.*, 1999] and gravity wave events [*Taori and Taylor*, 2006].

2.2. Stability Analysis

In this work several parameters are shown which can indicate the presence of instabilities or evanescent waves. While these have been discussed previously [*Beer*, 1974; *Gossard and Hooke*, 1975; *Hecht et al.*, 2002, 2005, 2007] they are reviewed below.

2.2.1. Richardson Number, *Ri*

Richardson [1920] showed that the stability of atmospheric regions is easily quantified by the Richardson number, *Ri*, which is given by

$$Ri = \frac{N^2}{(\mathrm{d}U/\mathrm{d}z)^2} \tag{1a}$$

$$Ri = \frac{(g/T)(\mathrm{d}T/\mathrm{d}z + g/C_p)}{(\mathrm{d}U/\mathrm{d}z)^2} \tag{1b}$$

where N is the Brunt-Väisälä frequency and $\mathrm{d}U/\mathrm{d}z$ is the horizontal wind shear defined as the variation of the horizontal wind, U, as a function of altitude, z. The square of N is given by the numerator of equation (1b) where T is the temperature, $\mathrm{d}T/\mathrm{d}z$ is the vertical temperature gradient, g is the gravitational acceleration, and C_p is the atmospheric specific heat at constant pressure. The quantity g/C_p is the adiabatic lapse rate which is typically about 9.5 K/km in the 85 to 90 km altitude region.

As noted in section 1, classically, there are two instability regimes that can occur. When *Ri* is between 0 and 0.25 a dynamical instability is likely to occur which leads to the formation of KHI billows. However, if N^2 is less than zero, which occurs when the atmospheric lapse rate exceeds the adiabatic lapse rate, a CI is likely to occur.

Examples of KHI features seen in OH images with coincident lidar data are shown in *Hecht et al.* [2005] and *Li et al.* [2005b, 2005a]. Examples of CI features seen in OH images with coincident lidar data are shown in *Hecht et al.* [1997] and *Li et al.* [2005b].

In this work the lidar data are used to determine the temperature profile, the MR data provide the wind shear, and the ANI images show if instability features exist.

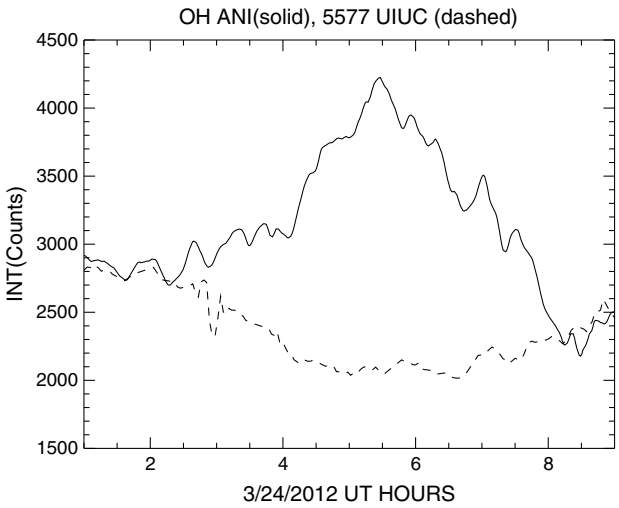

Figure 1. The solid line is a plot of the intensity in a 64 by 64 pixel box (from the middle row top column) in the raw ANI OH image (after flatfielding). The dashed line shows the OI(5577) Greenline intensity from the UIUC photometer scaled to match the ANI intensity at 2 UT.

3. Results

3.1. Overview From Airglow Image Data

The TOMEX experiment results suggested that instabilities form more readily when the background atmosphere is close to instability due to the presence of either a wind shear or a steep temperature gradient induced by large-amplitude AGW or tide [*Hecht et al.*, 2004c; *Liu et al.*, 2004]. Thus, Figures 1 to 3 investigate the state of the atmosphere from 1 to 9 UT on 24 March 2013 using OH image data.

Figure 1 shows plots of the OH intensity (OHI) from the ANI data and the corresponding OI(557.7 nm) brightness from the MCP. The MCP brightness data are arbitrarily scaled to match the ANI count data at just before 2 UT. After 2 UT the trend of the two data sets diverge with the OHI data increasing and the OI(557.7 nm) data decreasing. At 4 UT there is a sharp increase in the OHI and a corresponding decrease in the OI(557.7 nm). By 8 UT they have returned to the same relative count level.

These data can be interpreted as there being one or more waves with similar vertical wavelengths present. Given that the OHI and OI(557.7 nm) oscillations are out of phase and that there is a nominal separation between the emission layers of around 10 km [*McDade et al.*, 1986, 1987], the vertical wavelength of the wave causing the oscillation is around 20 km. These data also suggest that the event that begins at 4 UT peaks 1.5 h later and has an observed period near 3 h. The fractional amplitude in the OHI data of this 3 h wave is about 30% of the mean OHI. However, given that the OHI intensity depends not only on atmospheric density perturbations but also on chemical effects [e.g., *Schubert et al.*, 1991], there is some ambiguity as to the resultant atmospheric density perturbation. It is also interesting to note that the count levels at 9 UT are less than those observed at 2 UT. While this could be due to a decreases in atomic oxygen through the night (resulting in less OH production), this could also be consistent with the presence of a semidiurnal or diurnal tide.

An alternative way of assessing background waves in the atmosphere is to examine the OH temperature fluctuations. While these measurements tend to be of lower signal to noise than the OH intensity observations (since two measurements have to be divided by each other [*Taylor et al.*, 2001]), this does give a direct measure of the gravity wave amplitude and structure underlying the fluctuation in airglow intensity. Figure 2 presents results from the MTM. This shows more clearly that the oscillation that begins around 4 UT is due to a wave that is not associated with whatever (tidal oscillation or composition) is causing the change in background intensity from 2 to 9 UT. Furthermore, the observation of a large change in the background temperature from 2 to 9 UT is very consistent with a tidal origin for that feature since a

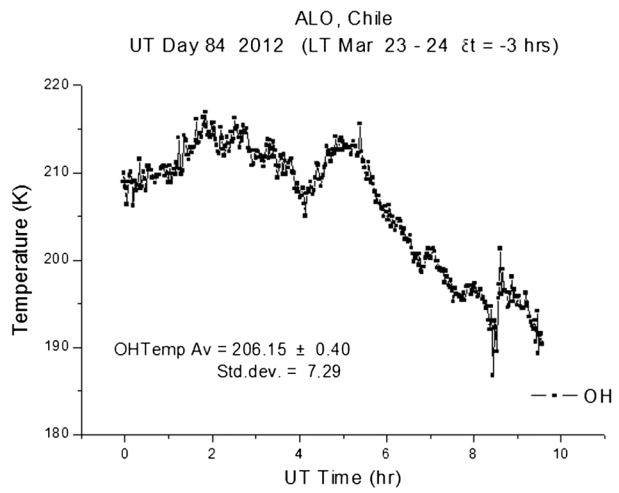

Figure 2. Plot of the OH temperature versus time from the MTM.

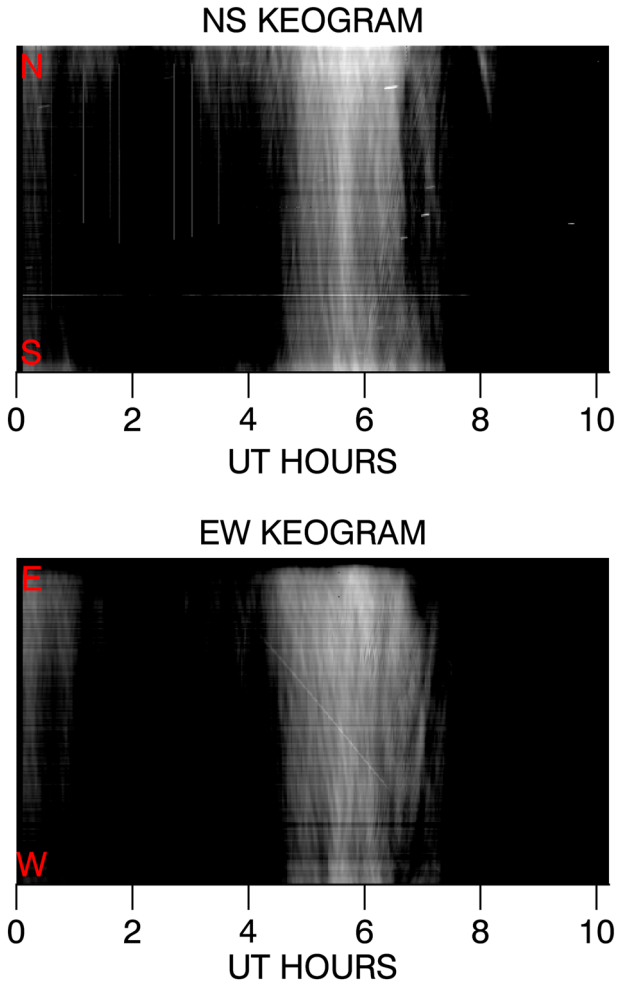

Figure 3. OH keograms in the NS and EW directions, as a function of UT, from ANI.

composition change is not expected to cause an oscillation in temperature. The oscillation that begins at 4 UT appears to have a period (between the beginning and ending of this wavelike feature) of 2 to 3 h and rides on top of the tidal decline. The fractional amplitude of this wave is about 3%. From this and the OHI amplitude one can determine the magnitude of the Krassovsky ratio [*Schubert et al.*, 1991], i.e., the ratio of the amplitude brightness perturbation to the temperature perturbation, to be 10 by dividing 30 by 3%. Based on Figure 16 of *Schubert et al.* [1991] this ratio is consistent with a multihour gravity wave oscillation.

The propagation direction of waves with wavelengths much larger than the instrument field of view is often determined using keograms. A keogram is created by choosing one (or more) columns or rows of an image and plotting this as a function of time. Since the imaging instruments are nominally aligned in the north-south direction, a column keogram provides a view of features moving from north (top of keogram) to south (NS) while a row keogram provides information on east (top of keogram) to west (EW) motions. Because stars move slowly from east to west the EW keograms can show star motions as diagonal lines.The two panels in Figure 3 provide the NS and EW keograms from ANI.

The contrast of the keograms was adjusted to emphasize the passage of the large signal wave between 4 and 7 UT. In the NS keogram it appears that both the N and S portion see the wave feature at about the same time. However, in the EW keogram the feature definitely appears in the east before the west. The time difference is about 1700 s. Assuming a distance of 120 km between the top east and west pixels gives a measured phase speed of around 70 m/s. Adjusting the contrast of the NS keogram suggests that there is a slight tilt in the phase front so that the wave may not be moving directly in the EW direction but slightly ENE to WSW. With that speed and a 2.5 h period the horizontal wavelength of this feature is about 600 km. However, these numbers are best estimates, given the uncertainty (at least +/− 10 m/s) of the phase speed.

3.2. Overview From Lidar and Radar Data

The airglow data in the previous section showed the presence of a large-amplitude wave, with a horizontal wavelength near 600 km, passing through the OH airglow layer from about 4 to 7 UT. Figure 4 presents four panels of data from the lidar and the MR that provides information on the vertical structure of the atmosphere during that period.

Figure 4 (top left) presents the temperature structure (in the vertical) from the lidar data. Here the temperatures are derived from smoothing over five 0.5 km bins and three profiles in time on either side of the designated time. Because there are a few times where the lidar did not obtain data this is equivalent to smoothing over approximately 20 min although for the profiles around 6 UT this reduces to 10 min. These data suggest that the atmospheric temperature within the OH airglow layer peaked around 5 UT consistent with Figure 2. While the peak temperature of ≈ 240°, at just below 85 km, is somewhat higher than the

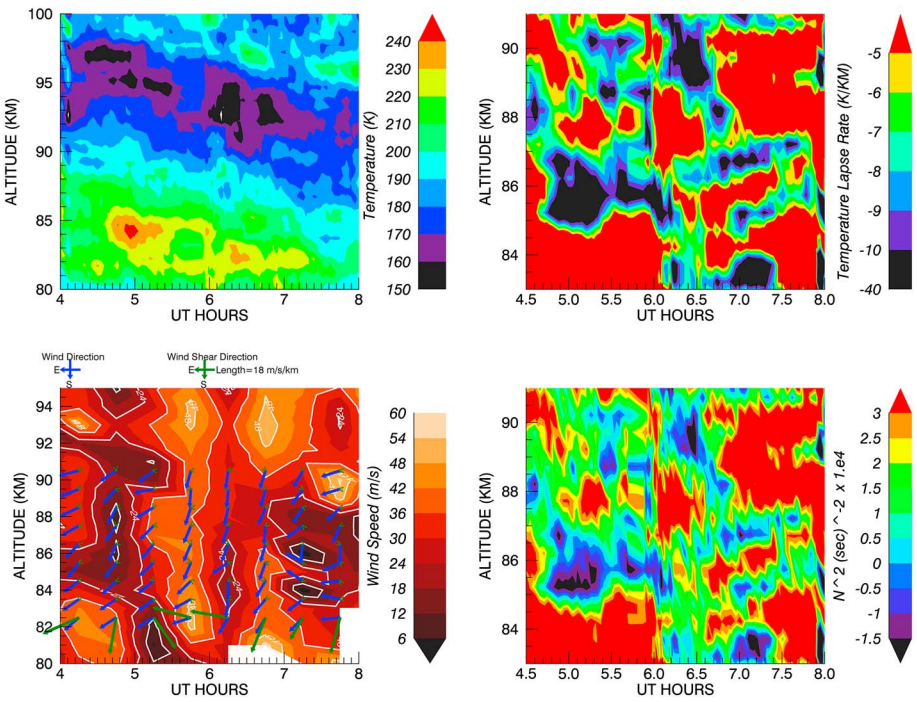

Figure 4. (top left) Lidar temperature data. (top right) N^2. (bottom left) Wind speed (contours) and direction (blue arrows) from the meteor radar and the shear (green arrows) derived from those data. (bottom right) N^2. The following smoothings are used. Temperature: approximately 10 min × 1 km altitude. Lapse rate: 20 min × 2 km bins. N_2 derived from temperature and lapse rate. Winds: raw data at 0.5 h and 1 km intervals.

215 K reported in Figure 2, those OH data are an average of the entire layer which nominally peaks at 87 km with a full width at half maximum (FWHM) of 10 km. Thus, one would expect the OH layer temperature to be somewhat lower.

Corresponding to this temperature peak is a minimum at 95 km, suggesting the presence of a wave with a vertical wavelength just over 20 km, again close to what was inferred from the airglow results. Such a wavelength is close to the expected wavelength of the diurnal tide and a long period descending layer can easily be seen in this lidar temperature plot. However, given the likely presence of the diurnal and semidiurnal tides and the short length of the lidar time series, it is difficult to unravel these waves from just this plot. Of additional interest to this study though is that the peak around 5 UT seems especially strong and somewhat isolated suggesting, as does the airglow data, that there is a shorter period wave present in addition to the tides.

Of greater importance to the existence of instabilities though is not the peak amplitude of the wave perturbations but rather the resulting temperature lapse rate shown in Figure 4 (top right). These rates are derived from smoothing the temperatures over five 0.5 km bins and five profiles in time on either side of the designated time. Because there are a few missing times this is equivalent to smoothing over approximately 30 min although for the profiles around 6 UT this reduces to 15 min. Nominally, the lapse rate will maximize between the altitudes of the amplitude minimum and maximum. Given the strong peak near 84 km it might be expected that the lapse rate will be greatest somewhat closer to the peak, and indeed, there is a large-amplitude negative lapse rate around 86 km. This large negative lapse rate persists around 86 km from 5 UT to about 730 UT. Figure 4 (bottom right) shows the resultant N^2. The adiabatic lapse rate is near 9.5 K/km so a negative lapse rate of greater magnitude would cause N^2 to be less than zero, resulting in a convectively unstable atmosphere. This panel shows that from about 5 to 730 UT there are small or negative values of N^2 just below the nominal peak of the OH layer at 87 km. Moreover, these large negative lapse rates appear to be descending in altitude at a rate consistent with them being caused by the descent of the 2 to 3 h wave discussed earlier. Because of the uncertainties in the data (and the necessity of performing considerable smoothing) one cannot determine whether the lapse rate is truly superadiabatic (less than −9.5 K/km), but nevertheless, the atmosphere appears to be close to being convectively unstable.

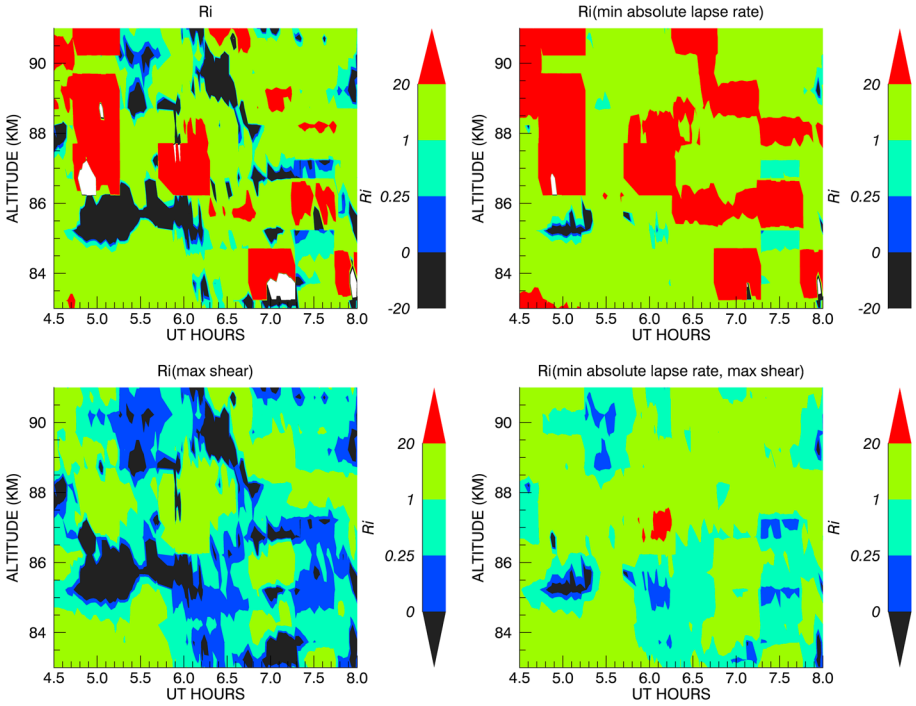

Figure 5. (top left) *Ri*. (bottom left) *Ri* assuming a one 1σ increase (5 ms/km) in the shear. (top, right) *Ri* assuming a one 1σ decrease (3 K/km) in the absolute value of the lapse rate with the sign unchanged. (bottom right) *Ri* assuming the shear increases and the magnitude of the lapse rate is smaller as in Figures 5 (top right) and 5 (bottom left).

Figure 4 (bottom left) shows (in red colors) the MR wind magnitudes along with blue arrows that show the direction of the wind and green arrows that show the magnitude and direction of the shear. Note that in this plot, east is to the left which matches the directionality of the images discussed later. Recall that the wind data are averaged over 30 min. In the period from 5 to 7 UT, at around 86 km, the winds are blowing between N to S and NW to SE with speeds of 30 to 40 m/s. This direction is nearly perpendicular to the direction of the 2 to 3 h wave. The shears are quite small at and above 87 km between 530 and 7 UT. Even at 86 km the shears are small, and thus, the shear magnitudes are uncertain due to 1σ uncertainties of 5 to 10 m/s/km in the shear magnitude.

The stability of the atmosphere is measured by *Ri* and depends on N^2 and the shear as shown in equations (1a) and (1b). Figure 5 presents four panels of *Ri* calculations. Figure 5 (top left) calculates *Ri* once every half hour using the closest N^2 value in time to the wind data. Here a convectively unstable region occurs below 86.5 km beginning at 5 UT that continues to about 6 UT. There is another convectively unstable region from 630 to 7 UT at 87 km. There is also a convectively unstable region near 89 km around 630 UT.

Given the large 1σ uncertainties in the shear (nominally 5 to 10 m/s/km) and the low values of the shear above 86 km (below 5 m/s/km) and the large error in the lapse rate (3 to 4°/km) there can be considerable uncertainty in the derived *Ri*. For example, the large stable region above 86 km between 5 and 6 UT is due to the low measured shears which will change when the error bars are applied. Similarly, the strong convectively unstable region would be less so if errors are considered. The other three panels in Figure 5 explore these uncertainties. Figure 5 (top right) shows the effect of a 1σ decrease in the magnitude of the lapse rate. Only a small region of instability remains, suggesting that the stability of the atmosphere is strongly controlled by the large lapse rate identified in Figure 4. Figure 5 (bottom left) shows the effect of a 1σ increase in the shear. As expected the dynamically unstable regions increase with the region from 84 to 87 km being either convectively or dynamically unstable from 5 to 730 UT. Figure 5 (bottom right) shows the effect of increasing the shear while decreasing the magnitude of the lapse rate. The unstable regions increase slightly, but clearly, the stability during these periods is more dependent on the lapse rate than on the shear.

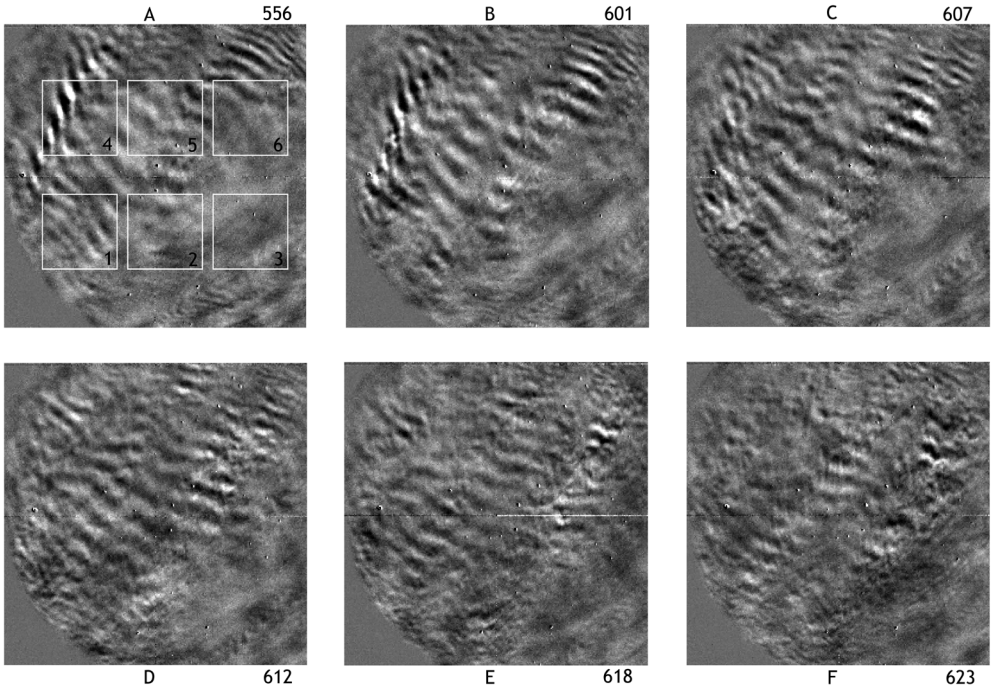

Figure 6. (a–f) This figure presents six 1 min difference images shown every 5 min starting at 556 UT through 623 UT. Each image has 256 × 256 pixels with a pixel being about 0.5 km square at 90 km altitude. Figure 6a in addition has six 64 × 64 pixel (32 × 32 km) boxes shown. Not shown in the center of each box is either a 4 × 4(2 × 2 km), 10 × 10 (5 × 5 km), or 16 × 16(8 × 8 km) region. North is on top, east is to the right, and the general wave motion is from the upper right to lower left.

3.3. Overview of Instabilities in the Airglow Image Data

The 1 min difference airglow images from ANI, presented in Figure 6, first show the presence of small-scale ripple features (presumably instabilities) beginning around 500 UT in the NE corner (upper left) of the image. This is perhaps to be expected, given that the OH layer first becomes strongly unstable around 5 UT, and a large-amplitude wave that could be contributing to making the atmosphere less stable (due to wave-induced variations in winds and temperature) also appears at 5 UT in the ENE. Ripple growth and decay continue until about 730 UT, and as this study is designed to investigate the decay of instabilities the six images shown in Figure 6 allow a measure of this process. To help the reader fully understand the motion of the waves, a movie of difference images is included as supporting information (Movie S1). The movie shows difference images at an approximate 4 s interval. A difference image is the difference between the image at the time and one about 60 s later. Individual difference images are discussed below.

Figure 6a is at 556 UT, and each of the other panels follow by between 5 and 6 min. Figure 6a shows six boxes which will be used for the quantitative analysis that follows below. The bottom row shows boxes 1 to 3 (from left to right) and the top row shows boxes 4 to 6. In Figure 6a box 3 is almost devoid of ripples and shows what a ripple free image looks like. Box 4 though shows the presence of very bright ripples, and the following will discuss their progression. These ripples have a nominal wavelength of about 8 to 9 km.

The bright ripples in box 4 first appeared about 540 UT. They are moving from the NW to SE (from the upper middle boundary of box 4 to the lower left corner of box 4) at about 40 m/s. This is consistent with the ripples being blown by the wind at some altitude between 85 to 89 km. Given that the 85 to 86 and 88 km altitude region is unstable at this time and that the ripples are quite bright, it is assumed that they are located around 87 km, the nominal peak of the OH layer. The phase fronts of this ripple sequence appear to rotate from the top of box 4 to the bottom of box 4, perhaps due to the directional shear that is developing near 600 UT at around 85 to 86 km altitude. What is more interesting though is what happens to the phase fronts as they move toward box 1 from box 4 in Figures 6b–6d. The well-organized phase fronts appear to suddenly break up and disappear. What remains are small disorganized (turbulent-like) features that do not resemble the ripple free box 3 seen in Figure 6a, and these features could be an indication of turbulence.

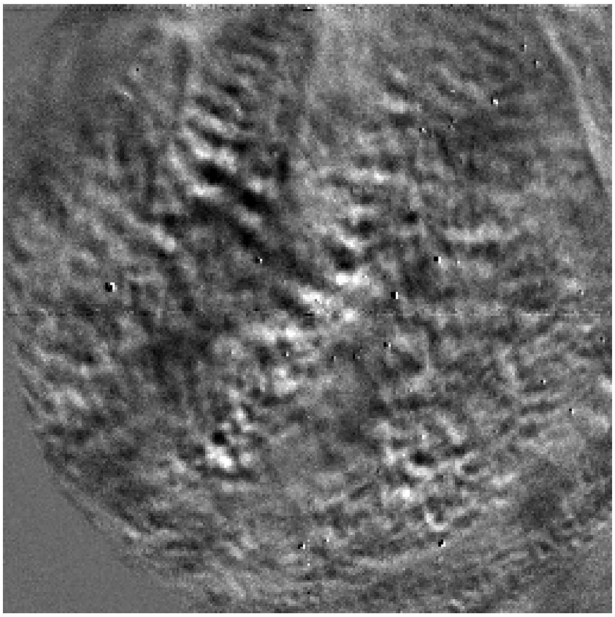

Figure 7. Similar to Figure 6, but only one image is shown at 641 UT.

A somewhat different ripple life cycle can be seen for those ripples approaching the top of boxes 5 and 6 in Figure 6a. These are traveling in the same direction and at a similar speed as the box 4 ripples. They show well-developed phase fronts. As they move toward the center of the image in Figure 6b they begin to break up. But before doing so, unlike the ripples in box 4, they develop a series of thin structures that are perpendicular to the main phase fronts. These are likely the secondary instability features described earlier and predicted by models [e.g., *Klaassen and Peltier*, 1985b, 1991; *Fritts et al.*, 1996; *Palmer et al.*, 1996]. By Figures 6e and 6f the organized structures (both primary and secondary) are mostly gone being partly replaced by smaller disorganized features. The transition, in the image data, from ripples with well-formed phase fronts to features that appear more disorganized, with weak or absent phase fronts, takes between 10 and 15 min. Some additional ripples appear subsequent to panel F but again decay.

Figure 7, at 641 UT, shows the very disorganized structures that remain due to the breakdown of ripples that appear after 630 UT. These features continue to move (presumably with the wind) and by 730 UT all of the disorganization is gone, having moved by the wind through the field of view, and the images resemble that seen in box 3 in Figure 6a.

The general picture that emerges from examining the images is that ripples with well-formed phase fronts form and grow mostly from the northern half of the images (boxes 4–6) and somewhat preferentially in the eastern half (box 4). Some evidence of well-formed phase fronts is apparent through much of the 6 to 7 UT period in boxes 4–6. In the lower half of the image (boxed 1–3) the ripples have mostly dissipated and more disorganized structures appear with little evidence of well-formed phase fronts.

3.3.1. Horizontal Wavelength of the Primary and Secondary Instability Features

As noted in section 1, one of the interesting results of the life cycle of KHI features seen over Maui was the unexpected small ratio of the primary to secondary horizontal wavelength [*Hecht et al.*, 2005]. In that study the ratio was near one while models such as *Klaassen and Peltier* [1985b] suggest values closer to four, with some variation depending on the Reynolds number of the atmosphere. For these results, the images shown in Figures 6 and 7 suggest that the primary wavelengths were larger than the secondary wavelengths and this is quantified by the following analysis.

Figure 8 shows part of a 60 s difference image where some ripples present near the center of the image (just below box 5) at around 628 UT. Two short lines are shown which are close to perpendicular and parallel to the main ripples. Figure 8 also shows plots of the airglow intensity along those two lines. For the main primary ripple phase fronts, the spacing is about 8.6 km while the secondary phase fronts have a spacing of around 3.1 km. The ratio of primary to secondary wavelength is 2.8. A similar result for the primary wavelength is found if the raw flatfielded image is used.

Table 2 also shows a similar analysis for two other periods. The first analysis is for the box 4 ripples at 552 UT a time at which no secondaries are seen. The primary wavelength is 8.3 km very close to what is seen at 629 UT. The second is for features in box 5 at 605 UT where secondaries do appear. The primary wavelength is 9.0 km, the secondary wavelength is 3.0 km, and the ratio of primary to secondary is 3.0. Thus, the primary wavelength is several times larger than the secondary wavelength for all three cases.

In a later section we will discuss these results in the context of both previous models and with new model simulations.

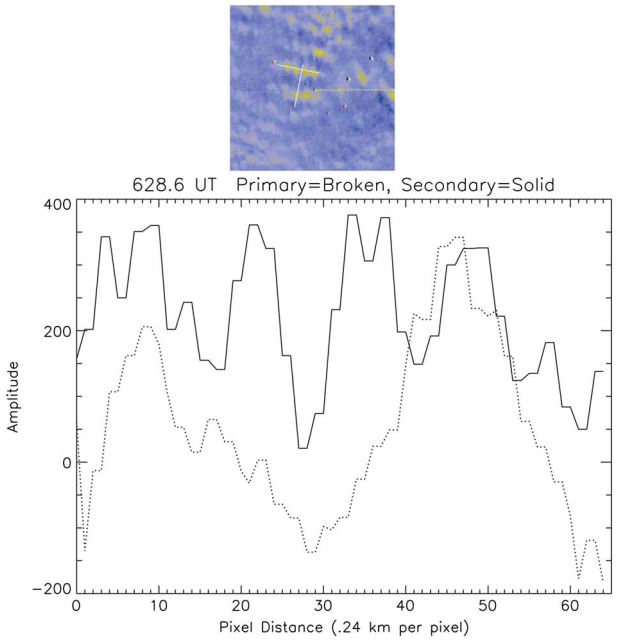

Figure 8. (top) One quarter of image at 629 UT. The white horizontal line at the center of the image is the center line of the image in the NS direction. Two short lines shown parallel and perpendicular to primary ripple phase fronts. (bottom) Plot of the intensity along the two lines. The dotted line shows the intensity from one primary peak to another while the solid line shows the intensity of a primary phase front modulated by the secondary phase fronts.

3.4. Entropy and Variance

The previous sections described the appearance of the images as organized or disorganized. There are several ways of quantifying this disorganization. One technique is to use the concept of the entropy of a distribution [*Shannon*, 1948; *Cover and Thomas*, 1991]. Entropy measures the randomness of the distribution and turbulence or disorganized structures would be expected to show an increase in entropy. A second technique directly measures the variance, σ^2, of the distribution. In this second technique the fractional magnitude of the small-scale fluctuations is computed from the ratio of σ of the small-scale features divided by the mean. However, entropy can also be used to calculate a variance but that calculation depends on the distribution of values. A convenient formula presented by *Shannon* [1948] gives the relation between entropy and variance for a normal distribution. Differences between the two measures of variances indicate to what extent the distribution of the measured values is close to normal.

In this section we present results of both techniques. The results will provide a measurement of the fractional fluctuation of the turbulent-like features, obtained from direct measurement of the variance in each of the six boxes as a function of time. We also derive the entropy at the same time to see how well these techniques agree. Because the entropy approach is less familiar these results are presented first.

Given a distribution of numbers with a probability density function P_i, defined as the probability of any number i being realized for any pixel, the entropy of such a distribution, designated here as H_n, is given in equation (2) by

$$H_n = -\sum_i P_i \ln P_i \tag{2}$$

$$e^{H_n} = 2^{H_2} \tag{2a}$$

$$H_n = (\ln 2)(H_2) \tag{2b}$$

Since a pixel is the basic unit from which the distribution is derived and H_n is expressed as a function of the natural logarithm, the units of H_n are nats (natural logarithm units) per pixel. To convert H_n to a log based 2 function, equations (2a) and (2b) show that H_n must be divided by ln(2). The units of H_2 (hereafter H) are in powers of 2 per pixel. Since a power of 2 is also called a bit the units then become bits per pixel. Note however that here the bit need not be an integer as is the more common usage.

Table 2. Ripple Horizontal Wavelengths (km)

Time (UT)	Primary	Secondary	Primary/Secondary
0552	8.3	None	NA
0605	9.0	3.0	3.0
0629	8.6	3.1	2.8
Model	8.5	NA	3–6

The meaning and use of the entropy concept for analyzing the ANI images require some explanation. First, note that H only depends on the variation of the distribution of pixel index value i, not its magnitude. So H for a uniform white or

black image is the same and is zero. Thus, H measures image uniformity. Second, the magnitude of H is larger when there is more variation in the pixel values, an indication that it can measure order and disorder. Third, note that the entropy of an image with say a house and a tree is the same if the pixel values making that image were randomly distributed throughout the image. An image of a house and tree represents large coherent structures while a random distribution may represent noise or small-scale structures. Thus, H does not necessarily reflect coherency. Fourth, of greater relevance for the ANI images is that a large-amplitude long wavelength wave will produce pixel values with a large distribution of intensity values thus causing H to become large. This can swamp the contributions of smaller more localized structure. Finally, there is a direct connection between H and σ^2. *Shannon* [1948] in his pioneering description of entropy and information showed that for a normal distribution H and σ^2 are related as given by

$$H = 0.5 \ln(2\pi e\sigma^2)/\ln(2). \tag{3}$$

Furthermore, for a given σ^2, a normal distribution gives the largest value of H. *Lazo and Rathie* [1978] gives the relation between H and σ^2 for other distributions.

Since one purpose of performing an entropy analysis is to quantify the presence of small-scale ripples and turbulent-like features the calculation of H must be modified. In previous studies [*Hecht et al.*, 2005] it was shown that rather than presenting raw flatfielded images, a better view of small-scale structure is by presenting difference images, produced by subtracting two images taken a minute apart. This is because differencing has the effect of removing the long period waves which tend to have the largest amplitudes, and these large waves reduce the contrast of the smaller structures.

We investigated several ways of modifying the image (via spatial or temporal filtering) prior to calculating H to see if any were more sensitive to the presence of small-scale (less than 20 pixel) structures. We will describe these efforts without showing plots of the results. The first calculation of H is from the raw flatfielded images and not surprisingly the presence of large-amplitude larger horizontal wavelength waves dominated H. Even this approach, though, revealed an increase in H between 530 UT and 7 UT. Next we calculated H for the 1 min difference images such as are shown in Figures 6 and 7. For these calculations, H clearly shows an increase between 530 UT and 7 UT. However, because long period waves still move over a minute they are not completely filtered out and the resulting H is still somewhat noisy. A better way of calculating H is to first form a new array consisting of all the differences between neighboring pixels. H is then calculated from this new array. Such a nearest neighbor pixel difference is simply a spatial filter which suppresses structures with large pixel wavelengths. Structures with a wavelength of 6, 20, and 30 pixels have their amplitude reduced to about 0.5, 0.15, and 0.1 of their original amplitude. When this technique was applied to either the raw flatfielded or difference images H increases during the 530 UT to 7 UT period where ripples and subsequent turbulent-like features become obvious. This latter approach was thus chosen. This spatial filter technique also allows a measure of the variance of the box region which can be calculated, from the variance of the spatial difference distribution. The mean of each box (before differencing) is also calculated.

Figure 9 shows the results for the H calculated using equations (2)–(2b) and this spatially differenced approach as applied to the raw flatfielded images. The raw flatfielded images were chosen because the potential problem of noise introduced by wave movement for difference images is eliminated. (Note, however, that raw flatfielded H values appear very similar to H obtained if the difference images were spatially filtered.) Clearly, there is an increase in H in the 530 UT to 7 UT period indicating that turbulent features occur during a period of increased entropy presumably caused by the presence of increased disorder due to the turbulence and small-scale ripples.

In each box the solid line plots generally show two peaks, one around 6 UT and one between 630 and 7 UT. Ripple events occur coincident with these peaks, and the first peak is more associated with the well-developed ripples while the second is more associated with disorganized (turbulent) features although some ripples are also present. Box 4 which has a stronger peak at 6 UT also shows the most well-developed ripples in the images around 6 UT and fewer turbulent structures in the images later after 630 UT. The box 3 images have almost no well-developed ripples between 6 and 7 UT and the H results show only the strong second peak in H. The box 2 images shows more of the turbulent features and also shows a stronger peak in H after 630 UT.

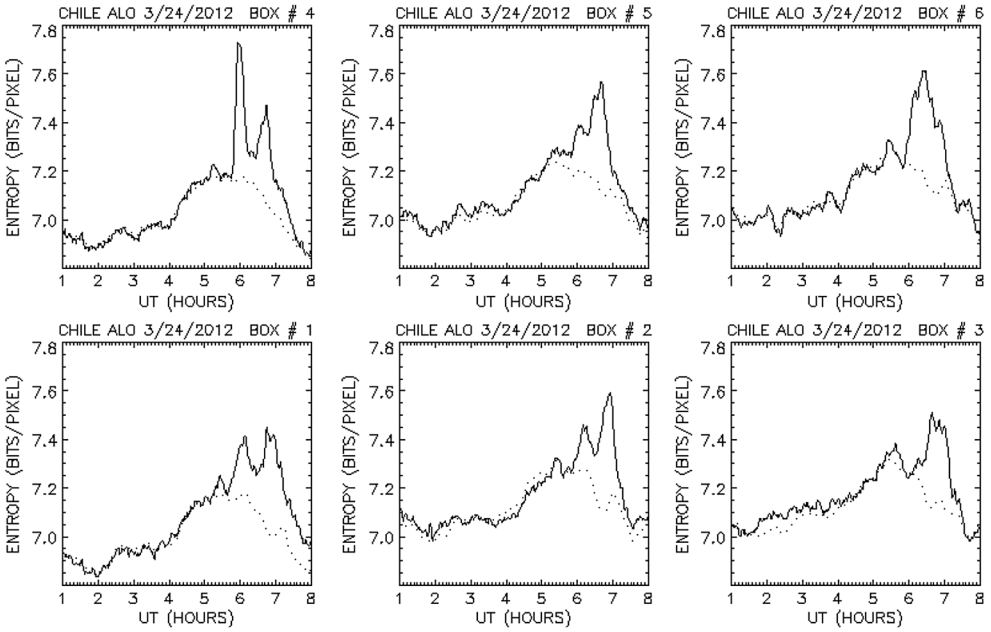

Figure 9. Six plots (one for each box) of the entropy of the shifted difference raw image as a solid line and the σ of the mean box intensity (in bits) increased by 1.45 bits as a dashed line.

To quantify this further we then compared these *H* values with those calculated from the variances using equation (3). We calculated the entropy for each box as a function of time and they matched very well providing these entropy values were reduced by 0.1 to 0.2 bits/pixel. Since noise due to counting statistics is typically Poisson distributed, which approximates a normal distribution, the difference is probably due to the distribution. To check this calculations of *H* were made from equation (3) for Poisson and Gaussian distributions, using the random function in Interactive Data Language with variances similar to those expected in the ANI images. The differences in *H* between the assumed Poisson and Gaussian distribution was on the order or less than 0.1 bit/pixel. The comparison of the two methods of calculating in the data suggests that the distribution is Poisson but close to normal.

Assuming a Poisson distribution of electrons in the detector, the mean value of each box would be equal to half the variance (since two pixels were subtracted) if each analog to digital unit (ADU) was an electron. However, several electrons are digitized to each ADU so if σ^2 in equation (3) is replaced by the measured mean, the calculated *H* values will be offset. In Figure 9 these *H* values, using the mean, are plotted, as a solid line, with a constant offset to best match the *H* values from equation (2). This comparison shows that the entropy due to the counting statistics is well below the measured entropy during the 530 to 7 UT period when the ripples/turbulent features appears.

The ratio of the mean to the variance is about 6 (in the periods away from the ripple period) in four of the boxes and 8 in two of the boxes. This is roughly equal to the number of electrons per ADU although if one takes the read noise into account and first subtracts an estimate of the variance due to that noise then the ratio of 6 increases to about 8. However, even without correcting first for read noise the ratios of 8 and 6 allows the use of the mean to estimate the variance due to the Poisson noise throughout the observation period.

The fractional fluctuations due to the turbulence alone then can be calculated by first subtracting from the total variance the variance due to Poisson counting statistics. The final result is obtained by taking the square root to get σ of the ripple/turbulent portion of the distribution and dividing by the mean. These fractional values are about 0.005 (0.5%) at the peak in box 4 at 6 UT and close to that value at the peaks in the 645 UT period where the turbulent structures dominate. These values may be somewhat underestimated since the spatial filtering does reduce the amplitude of features 6 pixels in size (about 3 km) by about a factor of 2. Smaller features though are not reduced as much.

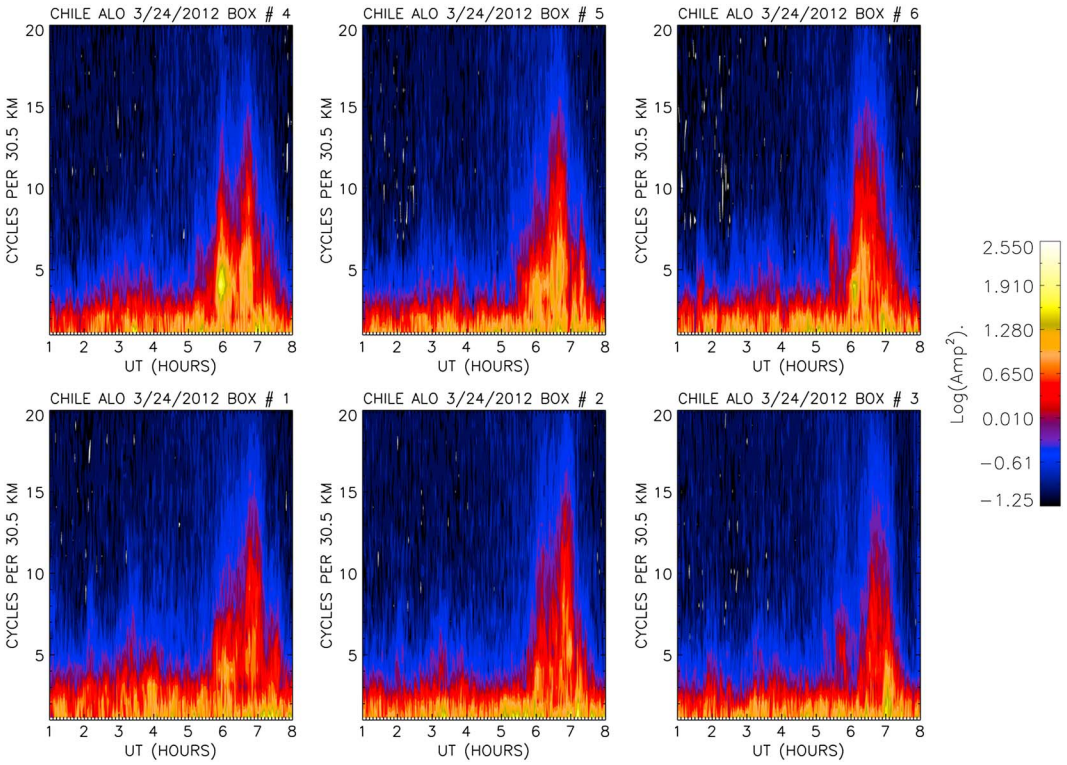

Figure 10. Six contour plots (one for each box) of the 2-D horizontal wave number spectrum as a function of time and wave number. The color bar shows the log of the amplitude squared of each spectral component and only applies within the contour plotting region.

To summarize, the entropy and variance analysis both show that during the periods where both the ripples and the turbulent-like features are seen, the amplitudes of these small-scale nonuniformities are well above the noise due to counting statistics.

3.5. Scale Size Using Fourier Transforms

In order to investigate the horizontal extent of the structures that are causing the increased entropy between 6 and 7 UT two-dimensional fast Fourier transforms (2-D FFTs) were taken of each box as a function of time. For a box with 64 pixels in the *i* direction and 64 pixels in the *j* direction a single mean horizontal scale was obtained following *Hecht et al.* [1994] by obtaining the power as function of pixel distance ($d = (i^2 + j^2)^{0.5}$). Note that we did not apply prewhitening (see *Hecht et al.* [1994] for a description of this technique) but we first subtracted the mean and then used a cosine taper window similar to that discussed in *Hecht et al.* [1994].

Figure 10 shows contour plots of the magnitude of these 2-D FFTs as a function of time and cycles per 30.5 km, the latter being the size of the box assuming that 64 pixels is equivalent to 30.5 km. This analysis was also done for both 30 s and 60 s difference images, and we show the results for the 30 s difference images as this filters out more of the larger structures allowing a better measure of the smaller-scale turbulence.

First look at box 4 in the top row. For the period around 6 UT, there is a peak present indicating a feature with a horizontal wavelength of four cycles per 30.5 km (four cycles per 64 pixels). Those are the well-formed phase fronts seen in Figure 6. Although there is a slight break around 630 UT (consistent with the entropy shown in Figure 9) there is also a second distinct peak (at about four cycles) from just after 630 to about 7 UT. This is consistent with the appearance of a second set of well-formed phase fronts in Figure 7 in the region occupied by box 4. What is interesting though is that the red level has now increased slightly extending to almost 15 cycles, an indication of the presence of smaller-scale structures. Boxes 5 and 6 in the top row also show strong peaks during the 6 to 7 UT period consistent with the assertion that the well-formed phase fronts appear in the upper half or the image.

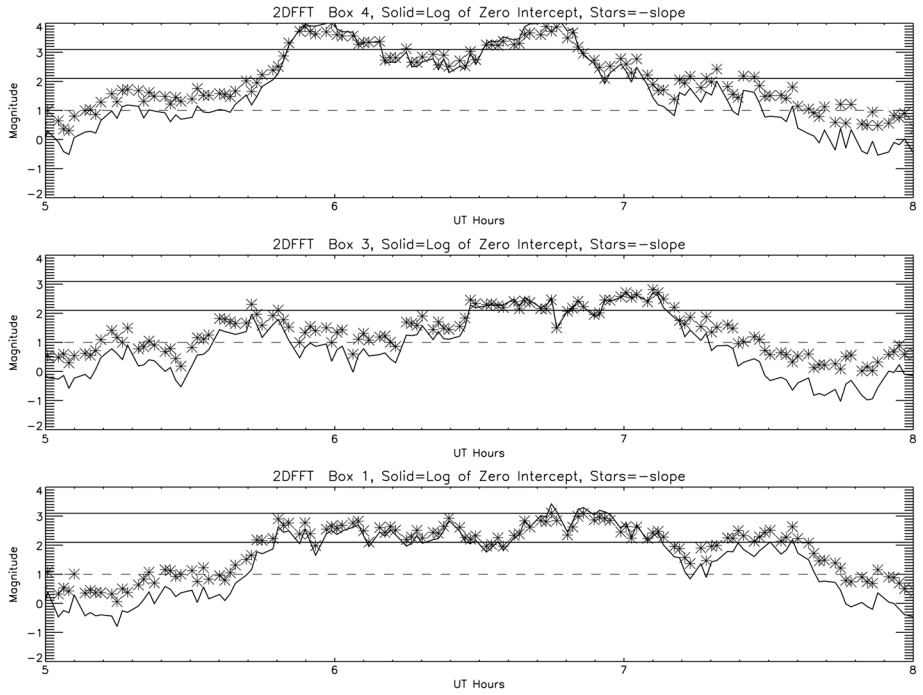

Figure 11. (top) Plots of the magnitude of the zero point intercept and the slope of the 2-D horizontal wave number spectrum in box 4 versus time. (middle) Same as Figure 11 (top) except for box 3. (bottom) Same as Figure 11 (top) except for box 1.

Next look at the bottom row. Box 3 shows no distinct feature at 6 UT and after 630 UT. When the 2-D FFT amplitudes increase after 6 UT there is no distinct feature but rather an indication of structures to 15 cycles. (The apparent structure at around 7 UT is a wave feature that passes through the image from W to E.) The results for box 2 are similar although there may be a weak peak just before 7 UT and there are some features at 6 UT but weaker than in box 5. Box 1 does some weak peaks near 6 UT, consistent with the ripples seen in Figure 6 but again weaker than in box 4.

However, all the bottom row boxes show evidence that the main contributor to the increase in *H* during the 6 to 7 UT period is the presence of smaller-scale features rather than the distinct features (around four cycles per 64 pixels) generally found in the upper half of the image. Furthermore, the smaller-scale features are stronger after around 620 UT than before.

3.5.1. Magnitude and Slope of the Fourier Transforms

To quantify this analysis better Figure 11 shows the results when a linear fit is applied to a log-log plot of the square of the amplitude (A^2) of the 2-D FFT components versus the spatial scale. The square of the amplitude should be proportional to the energy contained in each spatial scale. Three boxes, 1, 3, and 4, were analyzed with box 3 representing a location where well-formed ripples were not observed in the images, box 4 is a region where well-formed ripples appeared at least around 6 UT, and box 1 is the location that received the turbulent structures from the breakdown of the box 4 ripples.

For comparison with some modeling, we also computed the 1-D FFT by taking vertical slices (horizontal slices) through the 64 × 64 box, computing the FFT and then finding the average 1-D_y (1-D_x) spectra. In principle if the spectra were isotropic these could have been computed from the 2-D FFTs by integrating over the theta direction. Because the area in a differential element of area increases with increasing wave number magnitude the slope of the 2-D spectrum is deceased by 1; thus, the 1-D slopes computed this way should be the 2-D FFT slope plus 1. If this relation does not occur or the 1-D_x and 1-D_y slopes are different, this would suggest that some anisotropy is present in the images. Table 3 lists the slopes for the results discussed next.

Each of the panels of Figure 11 shows two plots, the magnitude of the log of the zero intercept of the linear fit, and the absolute value of the slope. The magnitude of the intercept is proportional to the magnitude of the energy at those scales. The slope was taken for structures with horizontal wavelengths between 6.1

Table 3. Measured Slopes Between 6.1 and 1.5 km

Box	Type	Spectral Type	Time (UT)	Slope	1σ
4	Diff	2-D	607–627	−2.83	0.07
4	Diff	$1D_x$	607–627	−1.10	0.08
4	Diff	$1D_y$	607–627	−1.59	0.02
3	Diff	2-D	628–657	−2.24	0.05
3	Diff	$1\text{-}D_x$	628–657	−1.40	0.07
3	Diff	$1\text{-}D_y$	628–657	−1.37	0.02
3	Raw	2-D	628–657	−2.26	0.26
1	Diff	2-D	607–627	−2.45	0.14
1	Diff	2-D	628–657	−2.60	0.05
1	Diff	$1D_x$	628–657	−1.43	0.13
1	Diff	$1D_y$	628–657	−1.56	0.04

and 1.5 km. The slope reflects the relative amplitude of the smaller scales, with a larger slope indicating that relatively fewer small-scale structures are present. (Note that all slopes are negative and the absolute value is shown for plotting.) The plots are shown from 5 to 8 UT which bound the period where ripples are present. At 500 UT and 800 UT no ripples are present and during those times A^2 is small (10^{-1}) and the slope is between −0.5 and −1.

First consider box 4 where, based on the images, well-formed ripples are present at around 6 UT. They begin to dissipate after 610 UT and are mostly gone by about 620 UT. Ripples appear again after 630 UT but are gone again after 650 UT. The results for A^2 in box 4 reflects what is seen in the images. It increases to 10^4 as the ripples appear, 5 orders of magnitude larger than at 5 UT before the period when ripples appeared. From 610 to 630 UT, the period where the ripples have decayed the magnitude is down by a factor 100 but that is still 1000 times higher than the prerippple period. When the ripples reappear after 630 UT A^2 increases again and after 650 UT A^2 decreases but still at a value much greater than the prerippple period at 5 UT. The decay back to the prerippple A^2 value takes about another half hour to 740 UT. Note that around 7 UT, a wave moves through box 4 which is reflected by the change in slope and increase in A^2.

The slope for box 4 follows a somewhat similar pattern to A^2. At 6 UT there is a peak slope of almost −4. Given that there is a nearly monochromatic ripple wavelength present and the possibility of spectral leakage [*Hecht et al.*, 1994], this slope probably is simply a reflection of the primary wave. However, after 610 UT, the period where the ripples are decaying, the magnitude of the slope increases and the mean value of the slope from 607 to 627 UT is $-2.83 +/- 0.07$. The $1D_x$ and $1D_y$ slopes are −1.10 and −1.59, respectively, and these results suggest significant anisotropy for this box. This is not surprising given the visible imagery showing that ripples are still present for some of this period.

Now consider box 3 where well-formed phase fronts are mostly absent and only disorganized structures are apparent from 6 to 620 UT. (At around 540 UT, a wave and some small ripples do pass through this box.) Recall from Figure 6 that at 6 UT, the disorganized structures have not appeared and at this time A^2 is low (about 0.1) and the slope is between −0.5 and −1. As the decaying ripples from box 1 appear in this box, A^2 rises and after 630 UT it is over 50. The average slope from 628 to 657 UT is $-2.24 +/- 0.05$. As noted above around 7 UT a wave moves through box 3 which is reflected by the change in slope and an increase in A^2. As in box 4 it takes about 30 to 40 min for A^2 to return to its prerippple value but this time is somewhat distorted by the passage of the wave at 7 UT. The $1\text{-}D_x$ and $1\text{-}D_y$ slopes are −1.40 and −1.37, respectively. Since the 1-D slopes are the same and equal to the 2-D slope plus 1 (within error), these results suggest that the structures are isotropic. This is not surprising given the visible imagery showing that only decayed ripples are present. For box 3, we also looked at the raw image, after flatfielding. This has a 2-D slope of −2.26 that is essentially the same as for the differenced images. However, the uncertainty is larger perhaps due to the flatfielding process. This does suggest though that the differencing is not distorting the spectrum.

Finally, consider box 1. This box is occupied mainly by the disordered structures from the decay of the ripples in boxes 4 and 5. From about 610 to 645 UT, this box sees few ripples. The value of A^2 is between 30 and 100 consistent with what is seen in boxes 3 and 4 during periods when the disorganized structures are present. From 607 to 627 UT, the 2-D slope is −2.45 while from 628 to 657 it is nearly the same at −2.60. The 1-D slopes are −1.43 and −1.56 for the *x* and *y* directions. Considering the errors, these values suggest a fairly isotropic set of structures with slopes somewhat between those found in boxes 3 and 4.

3.6. Wavelet Analysis for Ripple Periods

In order to quantify the periods of the ripples and of the disorganized features, a wavelet analysis was performed on the time series of the intensities for the six boxes following *Hecht et al.* [2007]. As in that paper, we also formed smaller regions within the main box on which a wavelet analysis was performed. For this

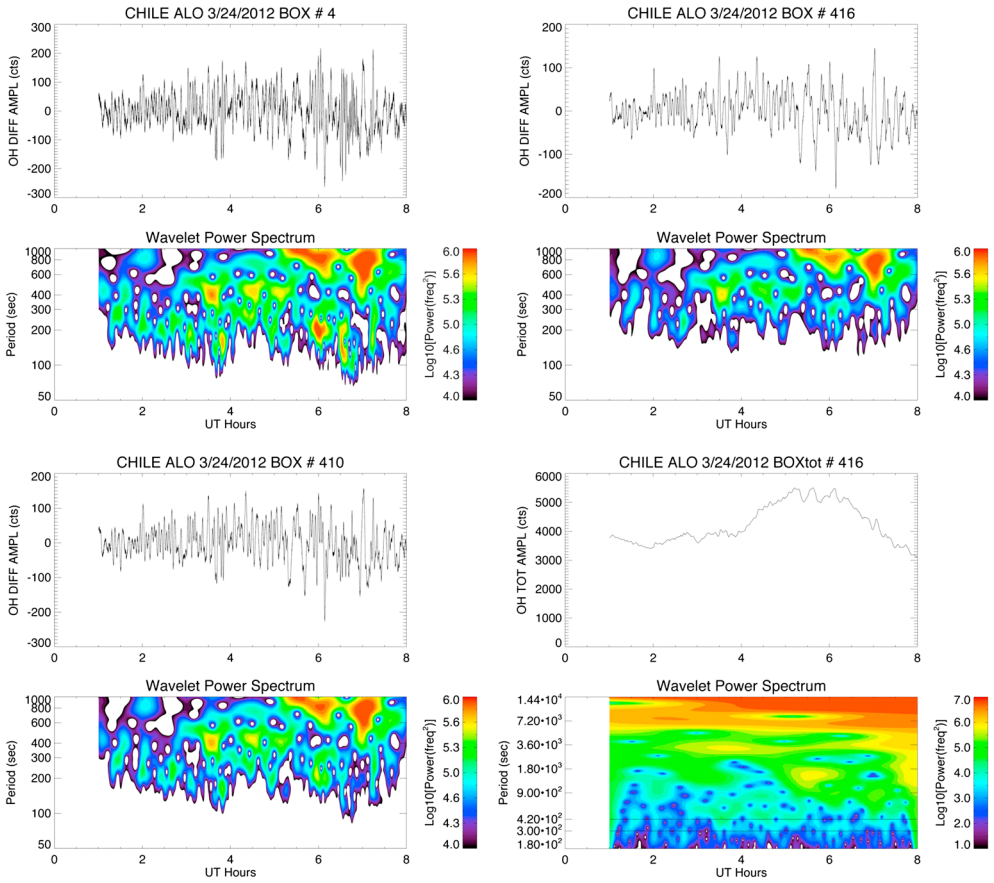

Figure 12. Wavelet analysis of box 4. See text.

investigation, the subboxes are 4 × 4 pixels (about 2 × 2 km), 10 by 10 pixels (about 5 × 5 km), and 16 × 16 pixels(8 × 8 km) in size. The smaller boxes see the small-scale sizes, whereas the 16 km box filters out the ripples.

Figures 12 and 13 show the results for boxes 4 and 2, each with four sets of wavelet power spectra. Each spectrum in the figure (color contour plot) has the corresponding time series plotted above. Three of the four sets are time series from the difference images. The fourth is from the raw image. The four sets cover 2 × 2 km (denoted as either box 4 or 2) top left, 5 × 5 km bottom left (box 410 or 210), 8 × 8 km top right (box 416 or 216), and 8 × 8 km for the raw images on the bottom right.

In Figure 12 which reports the box 4 analysis, consider the results for periods below 400 s. From Figure 6 the nominal Brunt-Väisälä period is above 300 s. The image data for box 4 in Figure 6 show well-developed ripples (8–10 km wavelength) around 6 UT. The wavelet analysis for this period (box 4 in the upper left) shows a strong peak at less than 200 s. This is consistent with ripples being blown through the box by the wind. (This effect was discussed for the Maui analysis reported in *Hecht et al.* [2007].) For the 8 × 8 km analysis (box 416), this signal has dissipated as would be expected by the filtering of an 8 km feature. However, the box 4 analysis (2 × 2 km) between 630 and 7 UT shows that there is an increase in the amplitude of structures with periods below 150 s. This is consistent with the smaller turbulent structures taking even less time to blow across the box.

The results for box 2 in Figure 13 show a very interesting result. Recall that the image data for this box in Figure 6 at 6 to 620 UT show some disorganized features along with decaying ripples. Figure 7 suggests mainly disorganized features at 641 UT, which persist to just before 7 UT. Based on the speed of these features a peak below 200 s would be expected. However, what is seen in the box 2 (2 × 2 km) analysis are peaks between 250 and 350 s. These cannot be due to motion across the box and below we speculate as

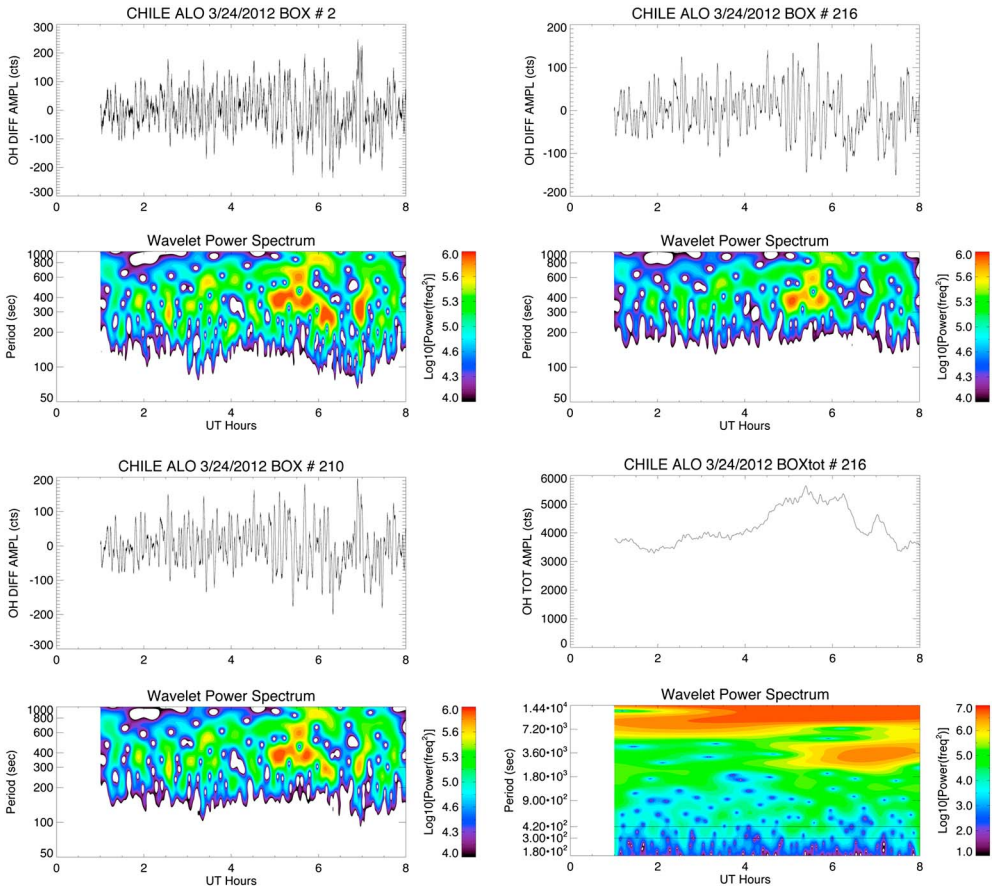

Figure 13. Wavelet analysis of box 2. See text.

their origin. They do, however, appear to represent a natural oscillation, whose physical meaning is not known, of the disorganized features. This is further discussed in section 4.3.

4. Discussion

The data presented above allow a study of two questions regarding the life cycle of the ripple features. One is whether the ripples form secondary instabilities more in agreement with model predictions than was found previously in the Maui-MALT study [*Hecht et al.*, 2005]. The second is what is the nature of the disorganized features seen after the well-formed ripples dissipate.

4.1. The Relation Between the Secondary and the Primary KHI Instabilities

The first question involves both the life cycle of the KHIs and the relationship between the KHI and secondary instability horizontal wavelength. This study focused more on the horizontal wavelengths, but the observed life cycle of the KHI features seem to be in reasonable agreement with the model predictions as summarized in *Hecht et al.* [2005].

In that study, however, the ratio of the horizontal wavelength of the primary KHI to the horizontal wavelength of the secondary instability was too small compared with the model predictions. In this study we have two sets of ripple structures, presumably either KHIs or CIs, that occur essentially in the same region. The ripples that pass through boxes 5 and 6 most certainly do form structures that are aligned perpendicular to the main phase front and are suggestive of secondary instabilities. This suggests that these ripple structures are indeed KHIs. The primary KHI horizontal wavelengths is close to 3 times greater than the secondary wavelength, a much larger value than the unity ratio seen in Maui study [*Hecht et al.*, 2005]. The models discussed earlier [e.g., *Klaassen and Peltier*, 1985b, 1991] predict primary to secondary wavelength ratios, for the fastest growing secondaries, of about 2 to 3 with the latter occurring at an *Ri* of 0. Thus, the ALO data are, in contrast to the Maui, consistent with the models and in fact suggest *Ri* values close to 0.

4.2. Are CIs Also Present in the Same Image

With respect to the nature of the ripples it is interesting to note that the ripples that pass through box 4 around 600 UT have nearly the same horizontal wavelength as the KHI ripples seen in box 5, but the box 4 ripples do not form a secondary instability before they decay. This has two implications. One possibility is that they are not KHIs but rather CIs. The differences between these two instability results are discussed from a modeling perspective in number of publications cited above [e.g., *Fritts et al.*, 1996; *Palmer et al.*, 1996; *Fritts et al.*, 1997]. The implications for airglow images is mentioned in those references and more directly in a number of observational studies [e.g., *Hecht et al.*, 1997, 2001; *Hecht*, 2004a]. Basically, it is expected that the CI would be formed perpendicular to a breaking gravity wave if it is a primary instability or perpendicular to a decaying KHI if it is a secondary instability. A KHI would form parallel to the breaking gravity wave. Given that the atmosphere is close to convectively unstable, it is certainly possible that the horizontal temperature gradient was such that in the box 4 portion of the sky *Ri* was less than zero. As noted above, the KHI secondaries appear to be consistent with an *Ri* close to 0 so it is not surprising that *Ri* is less than zero in another spatial position of the sky.

The fact that wavelengths and orientations of the ripples in box 5 and box 4 are the same suggests that the instability layer producing them is related. However, if they are separate types, KHI for box 5 and CI for box 4, then this is unusual as the orientation for convective instabilities might be expected, as noted above, to be perpendicular to those for a KHI [e.g., *Fritts et al.*, 1996; *Palmer et al.*, 1996; *Fritts et al.*, 1997; *Hecht et al.*, 1997, 2001; *Hecht*, 2004a]. Note though that the large wave causing the large-temperature lapse rate (and presumably responsible for a CI if it occurs) is moving nearly perpendicular to the ripple phase fronts and to the background shear. So it may be just fortuitous that the CI and KHI are aligned in the same direction.

Another possibility derived from the DNS analysis discussed below in section 4.4.2 and in the companion paper is that *Ri* is actually closer to 0.25 or the Reynolds number (defined below) is quite low (Fritts et al, 2014, available upon request). Such a large *Ri* or low Reynolds number would suppress the formation of secondaries based on model simulations presented in section 4.4.2 or in the companion paper (D. C. Fritts et al., 2014, available upon request) .

4.3. Production of Buoyancy Subrange Turbulence After Ripple Decay

The nature of the disorganized features appears to be related to the stability of the atmosphere. Between 6 and 7 UT, near the peak of the OH emission region, there are two periods, just before and after 6 UT and just before 7 UT where the atmosphere is either unstable (6 UT) or close to being unstable (before 7 UT). Between those two periods and after 7 UT the atmosphere is stable. The stability of the atmosphere is only being measured in the vertical so it is certainly possible that the atmosphere may be more or less stable at different locations. Thus, since the winds are blowing toward the SSW, some of what is observed may be forming in a region which has a slightly different stability than what is measured overhead.

Nevertheless, the image data, the entropy analysis, and the 2-D FFT results follow the same temporal pattern, two periods, close to 6 UT and to 640 UT, show different characteristics than the period in between. Interpreting this is complicated by a spatial difference, and the top half of the images shows different structures than the bottom half. It appears though that well-formed ripple features are dominating the entropy in the top half in much of the period between 6 and 7 UT although between about 620 and to just before 630 UT the well-formed phase fronts have dissipated even in the top half. The lower half of the image, as represented by box 2, sees mostly the dissipated phase fronts that appear "turbulent" like. The size of these features (1.5 to 6 km) places them in the buoyancy subrange for turbulent features following *Weinstock* [1978] and *Hocking* [1999]. Given that well-formed phase fronts do not occur, it seems possible that the atmosphere is somewhat more stable in the lower half than in the upper half where the background lapse rate is probably less negative and N^2 is probably higher. Thus, the Brunt-Väisälä period could be close to 300 to 350 s rather than the longer periods that occur when the lapse rate is large and negative. *Weinstock* [1978] has suggested that the oscillation period of the buoyancy range structures is quite close to the atmosphere's buoyancy frequency and it is speculated that is the explanation for the wavelet peaks between 250 and 350 s observed in box 2.

The work of *Weinstock* [1978] also discusses the expected values for the slope of the 1-D wave number spectrum which should nominally be −1.66 but can become somewhat less (between −1.33 and somewhat less than −2) depending on the value of the flux Richardson number. (The latter is somewhat different and usually a little larger than the *Ri* value reported in this work.) The conclusion of *Weinstock* [1978] though is

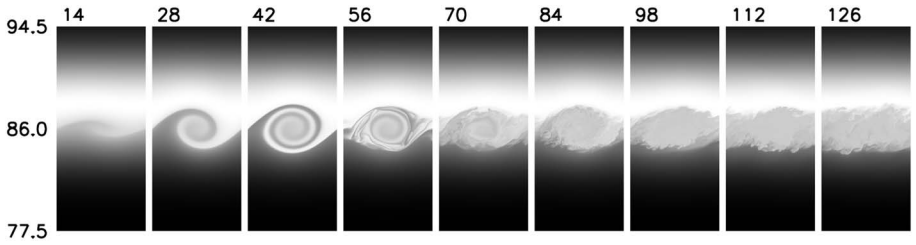

Figure 14. DNS airglow images at 8.5 horizontal × 17 km size. The time step is above each image, and 28 time steps is one buoyancy period. The images are centered at 86 km, and the shear layer is at the same altitude.

that if the slope is much more negative than −5/3, then this reflects a period of decaying turbulence while if the slope is less negative than −5/3 the turbulence is increasing. An earlier theory by *Lumley* [1964] had predicted slopes of −3. The values reported in this study for the 1-D slopes are between −1.2 and −1.6 for periods where disorganized structures occur. Since these values occur during periods where the primary KHI ripples have just decayed, it is not unreasonable to assume that there is a source of turbulence and the local *Ri* number may be low. Therefore, our results seem to be consistent with the model presented in *Weinstock* [1978].

4.4. Direct Numerical Simulation of Ripple Decay

To further investigate how ripples should decay Figures 14 and 15 show results from a Direct Numerical Simulation of the KHI formation and decay. Before describing those results the next section discusses the model formulation. A more complete discussion of the DNS results is given in the companion paper (Fritts et al., 2014, available upon request).

4.4.1. KHI Direct Numerical Simulation Model Formulation

Interpretation of our airglow observations is aided by a Direct Numerical Simulation (DNS) using a three-dimensional (3-D) code employed previously to explore primary and secondary Kelvin-Helmholtz instability (KHI) dynamics [*Werne and Fritts*, 1999, 2001; *Fritts et al.*, 2003]. The code solves the Boussinesq incompressible Navier-Stokes equations using pseudo-spectral methods in a Cartesian domain having periodic boundary conditions in the horizontal directions. (A pseudo-spectral method employs not only a spectral description of the dynamics but also Fourier transforms between spectral and physical space in order to perform computations of the nonlinear terms in physical space, as that is far more efficient than in spectral space.) This allows a compact representation of the dynamics and an accurate description of the secondary instability dynamics and associated turbulence and mixing typical of the mesopause region. The DNS simulations are characterized by two quantities, the Richardson number, *Ri*, defined in equations (1a) and (1b) and the Reynolds number *Re*. The *Re* number is given by $R_e = U_0 h/\nu$ where *N* is the Brunt-Väisälä frequency, U_0 is half the horizontal velocity across the shear layer, dU/dz is the vertical wind shear, *h* is half the shear depth, and ν is the kinematic viscosity. We assume a confined initial wind shear given by $U(z) = U_0 \tanh[(z - z_0)/h]$ where z_0 is the initial shear layer altitude.

The evolution of the KHI structures depends strongly on the chosen value for *Ri* while the scale size of the secondary instabilities depends strongly on *Re*. The KHI simulation presented by *Fritts et al.* [2012] applied to radar backscatter computations was performed for *Ri* = 0.05 and *Re* = 10,000 and yielded spanwise instability scales 2 times smaller than observed in the airglow images examined here. In that study the KHI billows evolved from fully formed into turbulent-like structures in around two buoyancy periods. The results in Fritts et al., 2014 (available upon request) show even smaller scales. Based on Figure 4 discussed above N^2 may be as high as 0.00015 s^{-2} during the 6 to 7 UT period where the ripples are observed. That value of N^2 is equivalent to period of just under 9 min. From the images in Figure 6 the ripple decay takes 15 to 20 min. Thus, for this study, an *Ri* of 0.05 and an *Re* of 2500 were chosen as possibly representative.

Given these values the other quantities are taken as follows. If N^2 is 0.00015 s^{-2} and *Ri* is 0.05, then the wind shear dU/dz is 55 m/s/km. This is much higher than observed although the radar observations do not have the altitude resolution to see a large shear confined to a narrow layer. Values of *Ri* that are large (say 0.25) would reduce the shear magnitude and would not rapidly produce the observed secondary instabilities. For this value of N^2 the Brunt-Väisälä (BV) period is 523 s.

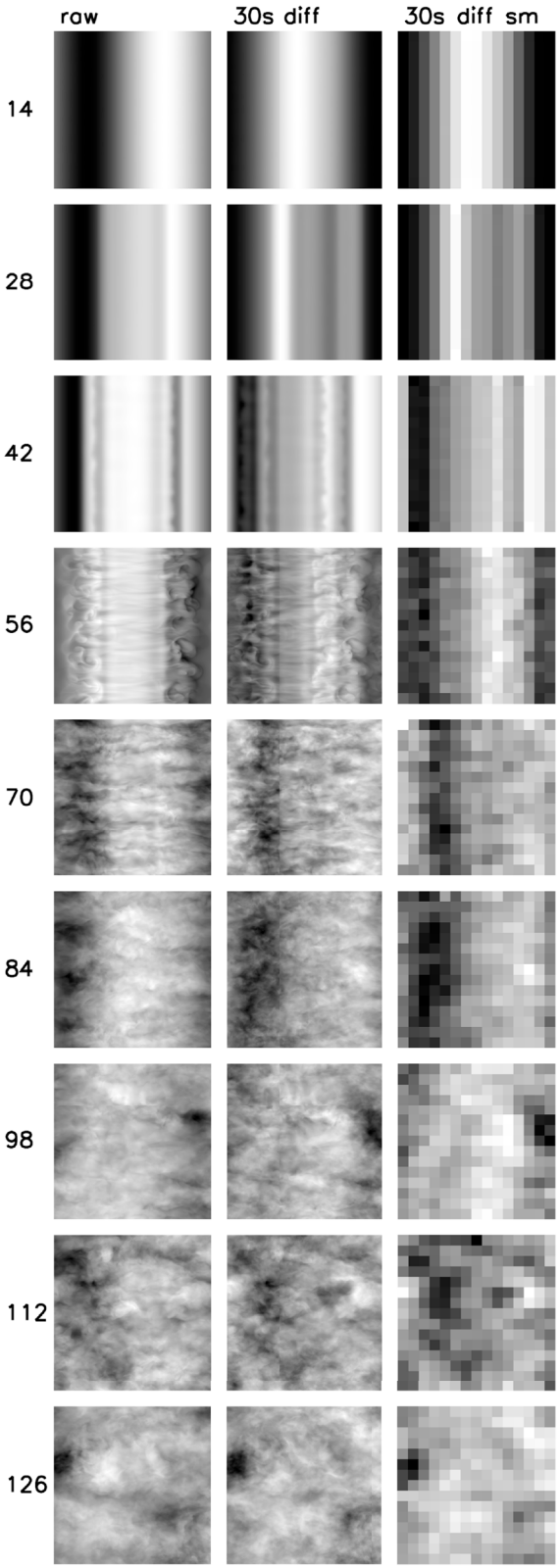

Figure 15. DNS airglow images at 8.5 × 8.5 km at approximately 11 m resolution. Images are shown at model time steps 14 to 126. Shown in three columns are the raw images, the difference of two raws taken 30 s apart (two model time steps) and that image degraded to approximately 500 m resolution.

The observed KHI billow wavelength is approximately 8.5 km, and the expected ratio of wavelength to shear half depth, h, is about 4π, for KHI billows at small Ri and large Re. This implies an initial shear depth of 2 h of about 1.35 km. Using these values for h and dU/dz, U_0 can be computed and found to be 37 m/s. The equation for Re then gives ν as 10 m^2/s. This value for ν is almost 4 times greater than expected at the OH airglow altitude of 87 km. This suggests that the KHI dynamics, especially the development of secondary instabilities at the observed scales, are influenced by the larger turbulent kinematic viscosity at these altitudes. While lower values for dU/dz would reduce the need to enhance the kinematic viscosity we note that *Hecht et al.* [2005] suggested that even higher values for ν and lower values of Re were needed to explain the lifetime of the observed KHIs seen in that study. The choice of these parameters will be commented in the next section.

Airglow influences of the KHI event shown above were simulated assuming that the KHI dynamics were sufficiently rapid to allow airglow brightness to be simply advected on these short time scales. This enabled representation of airglow brightness as a function of the potential temperature field predicted by the KHI DNS. A Gaussian brightness distribution was assumed for the undisturbed airglow layer centered at various altitudes relative to the initial shear layer, z_0, and having a full width at half maximum (FWHM) brightness of 7 km. Vertically integrated airglow brightness variations, and their spatial and temporal differences, along and across the KHI at various times were computed for displacements of the airglow layer center up to 5 km above and below z_0. While there are differences, the data suggest that the airglow layer is located either at or within 1 to 2 km of the shear layer. The DNS simulations are shown every 14 time steps where 28 time steps is one Brunt-Väisälä period. The model reports images at 750 by 750 pixels in the horizontal where 750 pixels is one wavelength.

4.4.2. KHI Direct Numerical Simulation Model Results and Comparison With the Images

Figure 14 shows cross sections of the airglow brightness as it is modified by the evolution of a KHI. In these images the x axis

Table 4. Modeled Slopes Between 4.3 and 1.4 km

Time (Model Units)	Spectral Type	Log10 Magnitude	Slope
56	2-D	−2.3	−2.20
56	1-D_x	1.28	−2.33
56	1-D_y	0.16	−0.30
84	2-D	0.60	−2.78
84	1-D_x	1.64	−2.85
84	1-D_y	0.42	−0.95
98	2-D	0.63	−2.92
98	1-D_x	1.15	−2.11
98	1-D_y	0.49	−1.00
112	2-D	0.20	−2.14
112	1-D_x	0.94	−1.71
112	1-D_y	0.50	−0.73
126	2-D	1.24	−2.90
126	2-D_R	0.82	−3.39
126	1-D_x	1.09	−1.85
126	1-D_{xR}	0.74	−1.89
126	1-D_y	0.91	−1.60
126	1-D_{yR}	0.89	−1.86

spans 8.5 km and the *y* axis spans 17 km with the center of the image at 86 km (the nominal center of the shear layer) and the airglow layer is taken as 2 km above that. One can see that at time step 42, the KHI is fully formed and begins to decay after that. From these images, coherent structures disappear by time step 98 or 112.

In order to compare with airglow images viewed from below, the airglow brightness is integrated in the vertical and images in the *x*-*y* plane are shown in Figure 15. The same sequence of time steps are shown and note that the spatial pixel size provided by the model is about 11 m, nearly 50 times smaller than the airglow camera pixel. Compared to the airglow images these images are showing more detail.

The first column shows raw images. At time step 42, the fully formed KHI phase front is aligned along the spanwise (*y* axis) while the direction of propagation would be along the streamwise (*x* axis). At time step 56 (0.5 a BV period later), clear secondary instability structures are seen aligned along the streamwise direction. These secondaries are clearly visible until time step 84. However, by time step 98, 1.5 BV periods later, turbulent-like structures are clearly dominant. The latter clearly dominate the image by time step 112. This means that the KHI structures, once secondaries are seen to form, should evolve to turbulent features in under 20 min (using a BV period of 523 s) consistent with the images displayed in Figure 6 and the time scales for decay from the 2-D FFT and entropy analysis of the images.

The next two columns show difference images comparable to the imager data. For these model images the KHI are advected and allowed to evolve over two time units where for a BV period of 523 s, two time units are 37 s. This evolved and advected image is then subtracted from the raw image to form a difference image. These difference images are shown in the second column. They show similar features to the raw images, suggesting that the differencing does not distort the KHI evolution. The third column then reduces the pixel resolution to 50 × 50 pixels giving a pixel size of around 500 m comparable to the size of a pixel in the ANI images. This shows to what extent the imager will miss structure in the KHI evolution. Clearly, there is much small-scale structure that is potentially missed.

To quantify the small-scale structure spanwise slices were taken through the second column images and then averaged. FFTs were calculated from these averaged slices. The thin streamwise strands in the time step 56 image had a nominal wavelength near 250 to 300 m (≈ wave number 30) although some even smaller scales were present. However, the results for time steps 70 and 84 also revealed distinct larger-scale peaks with wave numbers from 3 to 6 with the largest peak being around 3. Thus, the measured primary to secondary ratio of around 3 is consistent with the DNS model results although these results suggest a somewhat lower R_e based on the more detailed simulations described in Fritts et al., 2014 (available upon request). However, the airglow images could be missing considerable small-scale structure since the pixel size is only 500 m.

The primary purpose of performing the DNS analysis was to quantify the spectrum of buoyancy features. For these data, slopes were calculated for the 2-D and 1-D FFTs just as was done for the ANI images although for the model data the allowed wave numbers resulted in scale sizes between 4.3 and 1.4 km. The results for the slopes are given in Table 4. For the earlier time steps where the primary KHI phase fronts are easily seen in the model data, considerable anisotropy is apparent between the *x* and *y* directions as would be expected because of the presence of the primary. However, by time step 126 the primary is almost completely gone

Table 5. Model Fluctuations[a]

Time (Model Units)	Percentage (From *H*)	Percentage (From Variance)
14	2.7	4.7
42	2.1	2.8
56	1.22	1.34
70	2.03	2.25
98	1.27	1.34
112	0.94	1.04
126	1.18	1.22

[a]The second column uses equation (3) to calculate variance and the third column uses directly measured variance.

and there is only some small anisotropy with the mean 1-D_x and 1-D_y) slopes measured at −1.85 and −1.6, respectively. These values are somewhat lower though than the measured value of around −1.4.

The DNS analysis also allows a comparison of the magnitude of the fractional fluctuations seen in the model versus this observed in this study. They were calculated two ways by using the σ calculated from the entropy using equation (3) and by calculating the variance directly from the distribution. The magnitude from the variance is the number to be compared to the data while the difference between the values indicates if the distribution is close to normal. Table 5 shows those results, and the large difference between the two results at time step 14 is a consequence of having a distribution that is different from normal. However, by time step 42 when the KHI is fully formed, with secondary structures clearly visible, the two values are close suggesting the distribution is becoming normal-like. The magnitude of the fluctuation is about 0.028 (or 2.8%). However, as the secondaries decay at later time steps, the two values become closer indicating the distribution for the turbulence is close to normal. The magnitude of the fractional fluctuation of the turbulence drops to between 1 and 1.3%. This is about 2 times greater than what we observed with the much coarser resolution ANI images after considering that the ANI amplitudes are probably slightly underestimated.

The DNS model runs that were used in this comparison were part of a subset of runs that had been recently obtained. The variations of KHI evolution from the complete set are discussed more fully in the companion paper (Fritts et al., 2014, available upon request). Because the main interest in these DNS model runs is to observe the spectra of the large-scale buoyancy range features, and given the low-resolution wind data that were available, this study used the combination of *Ri* and *Re* that are close to those from the available data and also produced the closest match to the observed KHI evolution. A few comments can be made however about possible variation in the parameters. If the shear is indeed as small as the radar measurements suggest (less than 15 m/s/km), then for an instability at an *Ri* of 0.25 the BV period is about 14 min. The companion paper (Fritts et al., 2014, available upon request) shows that for such a high *Ri* the secondary amplitude would be small and probably not even visible in the airglow images. The smaller shear also affects the inferred value of ν via the *Re* value. Lowering the value of the shear nearly by a factor of 4 suggests either of the following. If *Re* is 2500, the kinematic viscosity would not need to be increased due to turbulence or if the higher turbulent viscosity of 10 m^2/s is retained, then the *Re* value is smaller and less than 1000. As the *Re* becomes smaller the secondary wavelength increases. Larger values of *Re* produce even smaller structures. Thus, in principle, a measurement of the secondary wavelength would allow an estimate of *Re* to be inferred, and if a good measurement of the shear is available ν could be inferred. However, to do either, higher-resolution spatial resolution images than provided by the present imager are needed.

5. Summary

This study reported on instabilities that are seen in the OH nightglow from 5 to 8 UT on 24 March 2012 over Cerro Pachon Chile, a period when a collocated Na lidar provided Na density and temperature data and a meteor radar provided atmospheric winds between 80 and 100 km.

The key findings are as follows.

1. During this period the wind shears in the peak altitude of the OH emission layer (at an altitude of 85 to 90 km) were small but the atmosphere had reduced stability because of the large negative temperature gradients in this altitude regime. Thus, regions of dynamical and convective instabilities might be expected to form depending on the magnitude of *Ri*.

2. The brightest instabilities that formed near 6 UT had horizontal wavelengths between 8 and 9 km and showed the subsequent formation of secondary instabilities suggesting an initial formation as a KHI.
3. The secondary instabilities had horizontal wavelengths about one third that of the primary KHI. This is different than what was found previously for the reported observations over Maui where the ratio of the two wavelengths was close to one. While the current results are in reasonable agreement with model predictions of KHI breakdown the observations still imply an increase in the turbulent viscosity from a nominal model atmosphere. In addition, given that almost all the Maui observations were devoid of secondary formation this also implies quite different background atmosphere with respect to *Ri* and *Re* over the two sites.
4. The brightest instabilities, seen near 550 UT, did not show these secondary features and may themselves have been convective instabilities although the DNS model simulations suggest that perhaps the *Ri* was actually higher in this region causing the secondaries to be suppressed.These bright instabilities also showed a rotation of the phase fronts away from the velocity vector suggesting perhaps the occurrence of a directional wind shear.
5. In both cases discussed in 3 and 4 the instability features decayed much more rapidly than those typically seen over Maui.
6. After dissipation of the instabilities smaller-scale features with sizes between 1.5 and 6 km were apparent in the images. Unlike the instability features that had well-formed phase fronts these features appeared much less organized. The size of the features places them in the buoyancy subrange. The slope of the square of the amplitudes associated with these features varied from −1.2 to −1.6 and is in agreement with the model of *Weinstock* [1978] if the turbulence is considered to be increasing. As determined from the image entropy analysis the ripple and turbulent-like features produced a fractional perturbation of the airglow of about 0.005.
7. DNS simulations produce secondary instabilities with scale sizes comparable to what is observed. However, the higher spatial resolution model shows even smaller features produced than can be seen in the images. The spectra of the buoyancy subrange scales are somewhat steeper than are observed. The fractional fluctuations seen in these simulations were about 2 times larger than were observed. A higher spatial resolution imager would help would resolve these differences.
8. Finally, we note that, regardless of the cause of the disorganized structures, similar looking features have been reported by *Yamada et al.* [2001] in their observations of the breakdown of 27 km horizontal wavelength gravity waves. When those waves first started to break structures parallel to the gravity wave phase, fronts appeared that are consistent with the formation of a KHI [e.g., *Hecht et al.*, 2001]. The phase fronts then dissipated into the same type of disorganized structures discussed here. The time scale for recovery was about 30 min. While there was no analysis of the nature of the disorganized structures the reporting of this event suggests that such features are not confined to the Chilean Andes and thus should be looked for at other sites.

Acknowledgments

We thank Steve Heathcote and the staff of the Cerro Tololo Inter-American Observatory for providing support for all the instrumentation and for the operations at the Andes Lidar Observatory. Support for J.H.H., L.J.G., R.J.R., and R.L.W. was provided by NSF grant 1110206 and by The Aerospace Corporation's SERPA program. Support for D.C.F. and K.W. was provided by NSF grants AGS 1261623, AGS-1242949, and AGS-1259136. P.D.P. and M.J.T. were supported by NSF grant 1110215. A.Z.L. was supported by NSF grants AGS-1115249 and AGS-1136278. S.J.F., F.A.V., and G.R.S. were supported by NSF grant 1110334. As noted in the text the movie file contains images used for much of the analysis in this paper. Any additional data can be obtained by contacting the lead author.

References

Beer, T. (1974), *Atmospheric Waves*, 300 pp., John Wiley, New York.

Browning, K. A., and C. D. Watkins (1970), Observations of clear air turbulence by high power radar, *Nature*, *227*, 260–263.

Carlson, C. G., G. R. Swenson, P. Dragic, and A. Liu (2005), Maui mesosphere and lower thermosphere (MALT) Na lidar enterprise, *Proc. SPIE 5979*, Remote Sensing of Clouds and the Atmosphere X, 59790W (01 Nov., 2005); doi:10.1117/12.625889.

Caulfield, C. P., and W. R. Peltier (2000), The anatomy of the mixing transition in homogeneous and stratified free shear layers, *J. Fluid Mech.*, *413*, 1–47.

Chandrasekhar, S. (1981), *Hydrodynamic and Hydrodynamic Stability*, 652 pp., Dover, New York.

Cover, T. M., and J. A. Thomas (1991), *Elements of Information Theory*, pp. 224–238, John Wiley, New York.

Davis, P. A., and W. R. Peltier (1979), Some characteristics of the Kelvin-Helmholtz and resonant overreflection modes of shear flow instability and their interaction through vortex pairing, *J. Atmos. Sci.*, *36*, 2394–2412.

Franke, S. J., X. Chu, A. Z. Liu, and W. K. Hocking (2005), Comparison of meteor radar and Na Doppler lidar measurements of winds in the mesopause region above Maui, Hawaii, *J. Geophys. Res.*, *110*, D09S02, doi:10.1029/2003JD004486.

Fritts, D. C., T. L. Palmer, O. Andreassen, and I. Lie (1996), Evolution and breakdown of Kelvin-Helmholtz billows in stratified compressible flows. Part I: Comparison of two- and three-dimensional flows, *J. Atmos. Sci.*, *53*, 3173–3191.

Fritts, D. C., J. R. Isler, J. H. Hecht, R. L. Walterscheid, and Ø. Andreassen (1997), Wave breaking signatures in sodium densities and OH nightglow: 2. Simulation of wave and instability structures, *J. Geophys. Res.*, *102*, 6669–6684.

Fritts, D. C., C. Bizon, J. A. Werne, and C. K. Meyer (2003), Layering accompanying turbulence generation due to shear instability and gravity wave breaking, *J. Geophys. Res.*, *108*(D8), 8452, doi:10.1029/2002JD002406.

Fritts, D. C., L. Wang, and J. Werne (2009), Gravity wave–fine structure interactions: A reservoir of small-scale and large-scale turbulence energy, *Geophys. Res. Lett.*, *36*, L19805, doi:10.1029/2009GL039501.

Fritts, D. C., K. Wan, P. Franke, and T. Lund (2012), Computation of clear-air radar backscatter from numerical simulations of turbulence. III: Off-zenith measurements and biases throughout the lifecycle of a Kelvin-Helmholtz instability, *J. Geophys. Res.*, *117*, D17101, doi:10.1029/2011JD017179.

Gardner, C. S., and A. Z. Liu (2010), Wave-induced transport of atmospheric constituents and its effect on the mesospheric Na layer, *J. Geophys. Res.*, *115*, D20302, doi:10.1029/2010JD014140.

Gossard, E. E., and W. H. Hooke (1975), *Waves in the Atmosphere, Atmospheric Infrasound and Gravity Waves: Their Generation and Propagation*, 456 pp., Elsevier, Amsterdam.

Hecht, J. H. (2004a), Instability layers and airglow imaging, *Rev. Geophys.*, *42*, RG1001, doi:10.1029/2003RG000131.

Hecht, J. H., R. L. Walterscheid, and M. N. Ross (1994), First measurements of the two-dimensional horizontal wavenumber spectrum from CCD images of the nightglow, *J. Geophys. Res.*, *99*, 11,449–11,460.

Hecht, J. H., R. L. Walterscheid, D. C. Fritts, J. R. Isler, D. C. Senft, C. S. Gardner, and S. J. Franke (1997), Wave breaking signatures in OH airglow and sodium densities and temperatures. 1. Airglow imaging, Na lidar, and MF radar observations, *J. Geophys. Res.*, *102*, 6655–6668.

Hecht, J. H., C. Fricke-Begemann, R. L. Walterscheid, and J. Höffner (2000), Observations of the breakdown of an atmospheric gravity wave near the cold summer mesopause at 54N, *Geophys. Res. Lett.*, *27*, 879–882.

Hecht, J. H., R. L. Walterscheid, and R. A. Vincent (2001), Airglow observations of dynamical (wind shear-induced) instabilities over Adelaide, Australia associated with atmospheric gravity waves, *J. Geophys. Res.*, *106*, 28,189–28,197.

Hecht, J. H., R. L. Walterscheid, M. P. Hickey, R. J. Rudy, and A. Z. Liu (2002), An observation of a fast external atmospheric acoustic-gravity wave, *J. Geophys. Res.*, *107*(D20), 4444, doi:10.1029/2001JD001438.

Hecht, J. H., A. Z. Liu, R. L. Walterscheid, R. G. Roble, M. F. Larsen, and J. H. Clemmons (2004b), Airglow emissions and oxygen mixing ratios from the photometer experiment on the Turbulent Oxygen Mixing Experiment (TOMEX), *J. Geophys. Res.*, *109*, D02S05, doi:10.1029/2002JD003035.

Hecht, J. H., A. Z. Liu, R. L. Bishop, J. H. Clemmons, C. S. Gardner, M. F. Larsen, R. G. Roble, G. R. Swenson, and R. L. Walterscheid (2004c), An overview of observations of unstable layers during the Turbulent Oxygen Mixing Experiment (TOMEX), *J. Geophys. Res.*, *109*, D02S01, doi:10.1029/2002JD003123.

Hecht, J. H., A. Z. Liu, R. L. Walterscheid, and R. J. Rudy (2005), Maui Mesosphere and Lower Thermosphere (Maui MALT) observations of the evolution of Kelvin-Helmholtz billows formed near 86 km altitude, *J. Geophys. Res.*, *110*, D09S10, doi:10.1029/2003JD003908.

Hecht, J. H., A. Z. Liu, R. L. Walterscheid, S. J. Franke, R. J. Rudy, M. J. Taylor, and P.-D. Pautet (2007), Characteristics of short-period wavelike features near 87 km altitude from airglow and lidar observations over Maui, *J. Geophys. Res.*, *112*, D16101, doi:10.1029/2006JD008148.

Hocking, W. K. (1999), The dynamical parameters of turbulence theory as they apply to middle atmosphere studies, *Earth Planets Space*, *51*, 525–541.

Klaassen, G. P., and W. R. Peltier (1985a), The evolution of finite amplitude Kelvin-Helmholtz billows in two spatial dimensions, *J. Atmos. Sci.*, *42*, 1321–1339.

Klaassen, G. P., and W. R. Peltier (1985b), The onset of turbulence in finite amplitude Kelvin-Helmholtz billows, *J. Fluid Mech.*, *155*, 1–35.

Klaassen, G. P., and W. R. Peltier (1991), The influence of stratification on secondary instability in free shear layers, *J. Fluid Mech.*, *227*, 71–106.

Klostermeyer, J. (1990), On the role of parametric instability of internal gravity waves in atmospheric radar observations, *Radio Sci.*, *25*, 983–995.

Lazo, A., and P. Rathie (1978), On the entropy of continuous probability distributions, *IEEE Trans. Inf. Theory*, *24*, 120–122.

Li, F., A. Z. Liu, G. R. Swenson, J. H. Hecht, and W. A. Robinson (2005a), Observations of gravity wave breakdown into ripples associated with dynamical instabilities, *J. Geophys. Res.*, *110*, D09S11, doi:10.1029/2004JD004849.

Li, F., A. Z. Liu, and G. R. Swenson (2005b), Characteristics of instabilities in the mesopause region over Maui, Hawaii, *J. Geophys. Res.*, *110*, D09S12, doi:10.1029/2004JD005097.

Liu, A. Z. (2009), Estimate eddy diffusion coefficients from gravity wave vertical momentum and heat fluxes, *Geophys. Res. Lett.*, *36*, L08806, doi:10.1029/2009GL037495.

Liu, A. Z., R. G. Roble, J. H. Hecht, M. F. Larsen, and C. S. Gardner (2004), Unstable layers in the mesopause region observed with Na lidar during the Turbulent Oxygen Mixing Experiment (TOMEX) campaign, *J. Geophys. Res.*, *109*, D02S02, doi:10.1029/2002JD003056.

Lumley, J. L. (1964), The spectrum of nearly inertial turbulence in a stably stratified fluid, *J. Atmos. Sci.*, *21*, 99–102.

McDade, I. C., D. P. Murtagh, R. G. H. Greer, P. H. G. Dickinson, G. Witt, J. Stegman, E. J. Llewellyn, L. Thomas, and D. B. Jenkins (1986), ETON 2: Quenching parameters for the proposed precursors of O2(b1 Σg+) and O(^{1}S) in the terrestrial nightglow, *Planet. Space Sci.*, *34*, 789–800.

McDade, I. C., E. J. Llewellyn, D. P. Murtagh, and R. G. H. Greer (1987), ETON 5: Simultaneous rocket measurements of the OH Meinel Δ = 2 sequence and (8,3) band emission profiles in the nightglow, *Planet. Space Sci.*, *35*, 1137–1147.

Miles, J. W., and L. N. Howard (1964), Note on a heterogeneous shear flow, *J. Fluid Mech.*, *20*, 331–336.

Orlanski, I., and K. Bryan (1969), Formation of the thermocline step structure by large-amplitude internal gravity waves, *J. Geophys. Res.*, *74*, 6975–6983.

Palmer, T. L., D. C. Fritts, O. Andreassen, and I. Lie (1994), Three dimensional of Kelvin-Helmholtz billows in stratified compressible flow, *Geophys. Res. Lett.*, *21*, 2287–2290.

Palmer, T. L., D. C. Fritts, and O. Andreassen (1996), Evolution and breakdown of Kelvin-Helmholtz billows in stratified compressible flows. Part II: Instability structure, evolution, and energetics, *J. Atmos. Sci.*, *53*, 3192–3212.

Peltier, W. R., and C. P. Caulfield (2003), Mixing efficiency in stratified shear flows, *Annu. Rev. Fluid Mech.*, *35*, 135–167, doi:10.1146/annurev.fluid.35.101101.161144.

Peterson, A. W. (1979), Airglow events visible to the naked eye, *Appl. Opt.*, *18*, 3390–3393.

Peterson, A. W., and L. M. Kieffaber (1973), Infrared photography of OH airglow structures, *Nature*, *242*, 321–322.

Richardson, L. F. (1920), The supply of energy from and to atmospheric eddies, *Proc. R. Soc.*, *A67*, 354–373.

Schubert, G., M. P. Hickey, and R. L. Walterscheid (1991), Gravity wave-driven fluctuations in OH nightglow from an extended dissipative emission region, *J. Geophys. Res.*, *96*, 13,869–13,880.

Scorer, R. S. (1969), The supply of energy from and to atmospheric eddies, *Radio Sci.*, *4*, 1299–1307.

Shannon, C. E. (1948), A mathematical theory of communication, *Bell Syst. Tech. J.*, *27*, 379–423.

Taori, A., and M. J. Taylor (2006), Characteristics of wave induced oscillations in mesospheric O_2 emission intensity and temperature, *Geophys. Res. Lett.*, *33*, L01813, doi:10.1029/2005GL024442.

Taylor, M. J., and M. A. Hapgood (1990), On the origin of ripple-type wave structure in the OH airglow emission, *Planet. Space Sci.*, *38*, 1421–1430.

Taylor, M. J., and M. J. Hill (1991), Near infrared imaging of hydroxyl wave structure over an ocean site at low latitudes, *Geophys. Res. Lett.*, *18*, 1333–1336.
Taylor, M. J., W. R. Pendleton Jr., S. Clark, H. Takahashi, D. Gobbi, and R. A. Goldberg (1997), Image measurements of short-period gravity waves at equatorial latitudes, *J. Geophys. Res.*, *102*, 26,283–26,299.
Taylor, M. J., W. R. Pendleton Jr., C. S. Gardner, and R. J. States (1999), Comparison of terdiurnal tidal oscillations in mesospheric OH rotational temperature and Na lidar temperature measurements at mid-latitudes, *Earth Planets Space*, *51*, 877–885.
Taylor, M. J., L. C. Gardner, and W. R. Pendleton Jr. (2001), Long period wave signatures in mesospheric OH Meinel (6,2) band intensity and rotational temperature at mid latitudes, *Adv. Space Res.*, *27*(6-7), 1171–1179.
Thorpe, S. A. (1968), A method of producing shear in a stratified flow, *J. Fluid Mech.*, *32*, 693–704.
Thorpe, S. A. (1973), Experiments on instability and turbulence in a stratified shear flow, *J. Fluid Mech.*, *61*, 731–751.
Thorpe, S. A. (1985), Laboratory observations of secondary structures in Kelvin-Helmholtz billows and consequences for ocean mixing, *Geophys. Astrophys. Fluid Dyn.*, *34*, 175–199.
Thorpe, S. A. (1987), Transitional phenomena and the development of turbulence in stratified flows: A review, *J. Geophys. Res.*, *92*, 5231–5248.
Vargas, F., G. Swenson, A. Liu, and D. Gobbi (2007), O(^{1}S), OH, and O_2(b) airglow layer perturbations due to AGWs and their implied effects on the atmosphere, *J. Geophys. Res.*, *112*, D14102, doi:10.1029/2006JD007642.
Walterscheid, R. L., and M. P. Hickey (2005), Acoustic waves generated by gusty flow over hilly terrain, *J. Geophys. Res.*, *110*, A10307, doi:10.1029/2005JA011166.
Weinstock, J. (1978), On the theory of turbulence in the buoyancy subrange of stably stratified flows, *J. Atmos. Sci.*, *35*, 634–639.
Werne, J., and D. C. Fritts (1999), Stratified shear turbulence: Evolution and statistics, *Geophys. Res. Lett.*, *26*, 439–442.
Werne, J. A., and D. C. Fritts (2001), Anisotropy in a stratified shear layer, *Phys. Chem. Earth*, *26B*, 263–268.
Woods, J. D. (1969), On Richardson's number as a criterion for laminar-turbulent transition in the ocean and atmosphere, *Radio Sci.*, *4*, 1289–1298.
Yamada, Y., H. Fukunishi, T. Nakamura, and T. Tsuda (2001), Breaking of small-scale gravity wave and transition to turbulence observed in OH airglow, *Geophys. Res. Lett.*, *28*, 2153–2156.
Zhao, Y., M. J. Taylor, and X. Chu (2005), Comparison of simultaneous Na lidar and mesospheric nightglow temperature measurements and the effects of tides on the emission layer heights, *J. Geophys. Res.*, *110*, D09S07, doi:10.1029/2004JD005115.